

## BAYESIAN SURFACE PHOTOMETRY ANALYSIS FOR EARLY-TYPE GALAXIES

D. H. STALDER,<sup>1,2</sup> REINALDO R. DE CARVALHO,<sup>1</sup> MARTIN D. WEINBERG,<sup>3</sup>  
SANDRO B. REMBOLD,<sup>4</sup> TATIANA C. MOURA,<sup>1</sup> REINALDO R. ROSA,<sup>1</sup> AND  
NEAL KATZ<sup>3</sup>

<sup>1</sup>*INPE/MCTIC, S. J. dos Campos, Brazil*

<sup>2</sup>*NIDTEC/FP-UNA, San Lorenzo, Paraguay*

<sup>3</sup>*University of Massachusetts/Amherst, USA*

<sup>4</sup>*UFRS, Rio Grande do Sul Brazil*

### ABSTRACT

We explore the application of Bayesian image analysis to infer the properties of an SDSS early-type galaxy sample including AGN. We use GALPHAT (Yoon et al. 2010) with a Bayes-factor model comparison to photometrically infer an AGN population and verify this using spectroscopic signatures. Our combined posterior sample for the SDSS sample reveals distinct low and high concentration modes after the point-source flux is modeled. This suggests that ETG parameters are intrinsically bimodal. The bimodal signature was weak when analyzed by GALFIT (Peng et al. 2002, 2010). This led us to create several ensembles of synthetic images to investigate the bias of inferred structural parameters and compare with GALFIT. GALPHAT inferences are less biased, especially for high-concentration profiles: GALPHAT Sérsic index  $n$ ,  $r_e$  and MAG deviate from the true values by 6%, 7.6% and  $-0.03$  mag, respectively, while GALFIT deviates by 15%, 22% and  $-0.09$  mag, respectively. In addition, we explore the reliability for the photometric detection of AGN using Bayes factors. For our SDSS sample with  $r_e \geq 7.92$  arcsec, we correctly identify central point sources with  $\text{Mag}_{\text{PS}} - \text{Mag}_{\text{Sersic}} \leq 5$  for  $n \leq 6$  and  $\text{Mag}_{\text{PS}} - \text{Mag}_{\text{Sersic}} \leq 3$  for  $n > 6$ . The magnitude range increases and classification error decreases with increasing resolution, suggesting that this approach will excel for upcoming high-resolution surveys. Future work will extend this to models that test hypotheses of galaxy evolution through the cosmic time.

*Keywords:* galaxies : structure - galaxies : photometry - methods : statistical

## 1. INTRODUCTION

The key to testing theories of galaxy formation and evolution is the full use of information in galaxy image data. Algorithmic approaches for describing two dimensional surface photometry profiles (e.g. SExtractor Bertin & Arnouts (1996), GIM2D Simard (1998), GALFIT Peng et al. (2002, 2010), 2DPHOT La Barbera et al. (2008), GALAPAGOS Barden et al. (2012), PyGFit Mancone et al. (2013), IMFIT Erwin (2015)) are based on maximum likelihood estimation (MLE), or more generally, optimizing an *objective* function that differentiates between two distributions. This approach has some significant limitations. Firstly, the estimated structural parameters are affected by random and systematic errors. For example, pixel integration, rotation and convolution techniques used to generate model predictions, as well as the background noise, contamination by nearby objects, initial guesses, the form of the objective function and the models themselves, minimization algorithms and image sizes (Häussler et al. 2007; Vikram et al. 2010; Guo et al. 2009; Simard et al. 2011; Mendel et al. 2014; Bernardi et al. 2017) may cause deviations from the correct model. Secondly, MLE is not independent of the parameter space coordinate system. For example, a simple change from a linear to logarithmic parametrization will lead to a different estimate. Therefore inferred galaxy properties using MLE fitting tools can be affected significantly (Bernardi et al. 2003; Hyde & Bernardi 2009) by seemingly innocuous changes in the problem definition. Thirdly, the MLE approach cannot easily select between various models for spheroids, bulges, discs and/or point sources given a particular galaxy image. In other words, MLE provides no relative measure of how well the model explains the data except in the special case of nested models. Finally, any preexisting knowledge (e.g. published results from related surveys) is not easily treated by the ML method. The Bayesian approach uses the laws of conditional probability to naturally incorporate prior knowledge of all aspects of the scientific problem, including both expert opinion and specifics of the model definition, to reduce the arbitrariness that often leads to bias. Specifically, Bayesian methods naturally incorporate random and systematic errors, lead to coordinate-independent estimates, and provide a robust framework for model comparison.

In recent years, Bayesian tools have become very popular for dealing with the drawbacks of frequentist approaches, partly due to advances in computer hardware speeds and the implementation of sophisticated sampling algorithms like Markov Chain Monte Carlo (MCMC) and partly due to the overwhelming evidence that this approach works! The astronomical community is on a *wave* of testing and developing new software tools to improve the accuracy of the inferred galaxy structural parameters and other photometric attributes and to choose the models that best describe their light distribution (Bouché et al. 2015; Robotham et al. 2017). Each implementation has its specific advantages and weaknesses. In this work we adopt GALPHAT (GALaxy PHotometric ATtributes); GALPHAT was the first parallelized code available and extensively tested considering simulated galaxy images (Yoon et al. 2010, hereafter YMK10). GALPHAT is a front-end application of a more general and pow-

erful tool called the Bayesian Inference Engine<sup>1</sup> (BIE; Weinberg 2013). BIE is an application based on a parallel MCMC algorithm that, for each parameter, gives the full posterior distribution and likelihood marginalization.

MLE packages provide a best-fit parameter value and, optionally, a covariance matrix at the ML value. A Bayesian inference, e.g. using GALPHAT, provides a probability distribution of parameter values, reflecting the improved constraints provided by the data given the prior distribution. Both of these describe values of the model parameters implied by the data. However, even in the simplest inference, we do not truly know the underlying model family. In more complex inferences, a complex galaxy formation hypothesis may provide a variety of possible model choices.

Similarly, astronomers typically use a variety of analytic light profiles. We often do not know which of our analytic models best explains a particular image and want to discriminate between possible models when different analytical forms describe physically distinct components, such as bulges and ellipticals (Sérsic law), discs (exponential) or active galactic nuclei (central point source), based on the data itself. Bayes Law allows us to pose an inference in the space of possible models. This yields a relative probability of one model over its competitors. This posterior odds ratio is often quoted in terms of the *Bayes factor*, assuming that all models are equally probable initially. The Bayes factor (BF) provide a mechanism that evaluates the evidence in favor of each considered model rather than only testing the goodness of fit. BFs are a natural method for model selection in the Bayesian context (Jeffreys. 1961; Kass & Raftery 1995; Wakefield 2013; Weinberg 2013). In this paper, we use GALPHAT and this Bayesian model-comparison approach for testing the hypothesis that early-type galaxies contain a point source typical of nuclear activity using Bayes factors. High resolution images obtained by the Hubble Space Telescope (HST) reveal fine details of galaxy structure. Previous studies have shown high correlations between nuclear activity of galaxies with galaxy structural parameters (Faber et al. 1997; Ho et al. 2003; Ravindranath et al. 2002; Ho & Peng 2001; Capetti & Balmaverde 2007; Hong et al. 2015; Bruce et al. 2016). However, separating the faint nucleus from the bright bulge is a difficult task. We will show that GALPHAT identifies weak AGN sources photometrically in images from the SPIDER sample (La Barbera et al. 2010). These images are selected to be normal early-type galaxies (ETGs) using SDSS eClass < 0 and fracDev<sub>r</sub> > 0.8. We show that the power of this approach dramatically increases for PSF scales significantly smaller than the half-light radius. Our SDSS images have relatively low resolution, but our results suggest that our methods will enable higher redshift AGN identification using upcoming high-resolution capabilities of the Thirty Meter Telescope (TMT), the Very Large Telescope (VLT) and the James West Space Telescope (JWST).

This paper extends our previous work (YMK10) by applying GALPHAT to a large sample of SDSS early-type galaxies (ETGs) and using Bayes factors to classify ETGs with and without nuclear unresolved sources. The paper is organized as follows. We

<sup>1</sup> This code is publicly hosted by Bitbucket: <https://bitbucket.org/mdweinberg/BIE>.

begin, in Section 2, with a brief description of GALPHAT and its application to our target sample. We present an automated pipeline, called PyPiGALPHAT, to analyze galaxy structural parameters, retrieve images from a given survey, generate configuration files, run SExtractor, and finally schedule GALPHAT analyses and manage acquired data from an HPC cluster. We explore the precision and reliability of our parameter inference and model comparisons by benchmarking on a synthetic catalog similar to our SDSS sample in Section 3. Specifically, we measure the bias and quantify the Bayes Factor reliability considering an ensemble of simulated galaxy images mimicking an SDSS galaxy sample and compare with GALFIT results. In Section 4 we present our findings for our target SDSS sample. We find that our ETGs are a bimodal population and correlate one of the modes with AGN activity using an WHAN-diagram analysis. We summarize our findings in Section 5.

## 2. INFERRING STRUCTURAL PARAMETERS USING GALPHAT

### 2.1. Overview

The objective function is central to optimization-based methods such as maximum likelihood and Bayesian posterior sampling. In both cases, an accurate result depends on a well-posed, accurate objective function. For Bayesian applications, the objective function is the true likelihood function: the probability of obtaining the observed pixel values,  $D$  given the model  $M$  and its parameter vector,  $\theta$ :  $L(D|\theta) = P(D|M, \theta)$ . Since most solid-state digital sensors count electrons, the probability for each pixel is a Poisson process whose predicted counts includes the production of electrons by photons and all other instrumental sources. For each pixel, the source prediction follows from a two-dimensional integration of the flux model convolved with the optical response function for the optics including effects of the atmosphere. The brute-force four-dimensional numerical quadrature is computationally unfeasible. Most algorithms use a combination of interpolation and DFT-based convolution to make this tractable. GALPHAT uses nested interpolation tables with FFT rotation and convolution. We have exhaustively checked the accuracy of this method with explicit adaptive four-dimensional quadrature. Some of these tests will be described in Section 3.2.

The astronomical source is described by a magnitude or flux value, a geometric center ( $X, Y$ ), a scale or half-light radius ( $r_e$ ), a sky model, and a variety of shape parameters that parametrize the light profile. For an ETG profile described by a Sérsic (1963) law, shape parameters include the Sérsic index ( $n$ ), axis ratio ( $q = b/a$ ), and position angle (PA). Assuming a simple flat sky background model with one parameter (SKY), we have eight parameters in all. As the Sérsic index increases, the profile increases in concentration; e.g.  $n = 1$  is the exponential disc and  $n = 4$  is the de Vaucouleurs (1948) profile. Late-type galaxies are often described by a bulge (Sérsic law) and a disk (exponential law). This adds four additional parameters: a bulge to total flux ratio, a bulge to disk length-scale ratio, and an additional axis ratio and position angle for the second component. This is a total of twelve parameters.



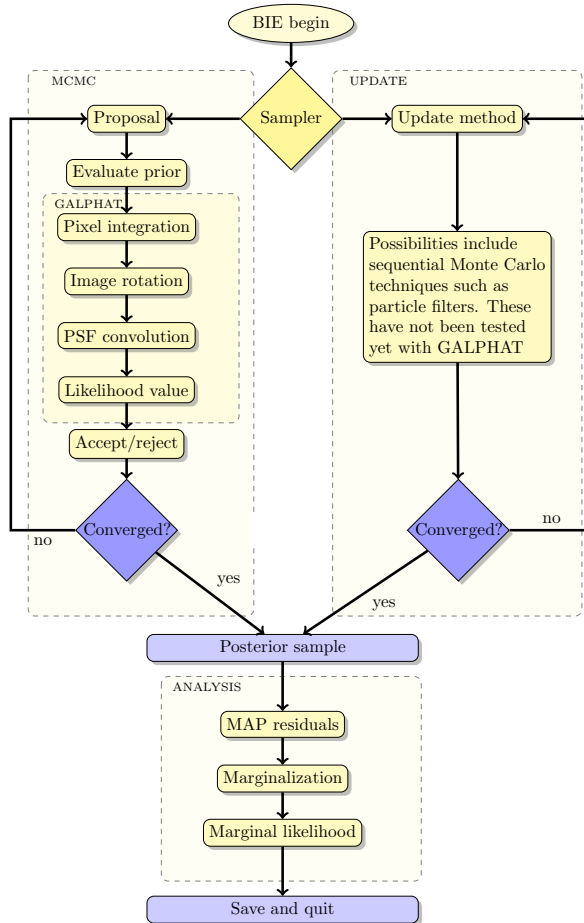


**Figure 1.** Graphical description of a posterior inference using BIE with GALPHAT. The BIE is a general platform for estimating high-dimensional posterior distributions using Markov chain Monte Carlo (MCMC) algorithms (left column) and non-Markov chain samplers based on the “update” feature of Bayes Theorem, such as sequential algorithms (right column). Here, GALPHAT provides the likelihood-function evaluations and may be used with many methods provided by the BIE. Since MCMC algorithms are the natural choice here, we highlight the location of the GALPHAT likelihood function in the computational flow.

GALPHAT is part of the Bayesian Inference Engine (BIE), a general parallel optimized software package designed to perform parameter inference and model selection (Weinberg 2013) on high-performance computing cluster hardware. Figure 1 shows an overview of all the steps involved in the Bayesian analysis of a galaxy image carried out in BIE using GALPHAT. BIE implements a variety of algorithms for sampling and estimated the Bayesian posterior distribution. To date these include Markov Chain Monte Carlo (MCMC) algorithms based on the Metropolis-Hastings concept and sequential Monte Carlo techniques based on the Bayesian update concept, such as particle filtering. To date, we have only tested GALPHAT using MCMC algorithms. For the work described here, we will use the differential evolution algorithm (Ter Braak 2006). This algorithm has the advantage of adaptively tuning the proposal step, removing one of the main stumbling blocks in the application of the naïve

Metropolis-Hastings-based method. The BIE also includes posterior analysis for both visualization and characterization. The BIE implements the marginal likelihood computation described in Weinberg (2012a) that we will use for Bayes factor computation and classification in Section 3.4. The fast and accurate likelihood algorithms implemented in GALPHAT allow one to probe the parameter space efficiently (YWK10). GALPHAT and the BIE produce a highly detailed description of the relationships between all model parameters implied by the data.

However, all of this extra information comes at a price: a full posterior simulation requires more likelihood evaluations than the traditional optimization approach. This application was, in part, our motivation for developing the BIE. Although a small number of model inferences are tractable on workstations and laptops, a large-scale campaign requires HPC hardware. For this work, we developed an automated pipeline, called PyPiGALPHAT, to streamline the work flow for an astronomical image survey. A detailed description of PyPiGALPHAT is presented in Appendix B.

Each image analysis begins with an initial estimate of the model parameters from the survey catalog. The posterior distribution describes the probability that our model’s parameter vectors describe the galaxy in light of the details provided by the observed data including any prior analysis by the catalog compilers. Although it is common to characterize the inference by its best fit, the real power in the Bayesian approach is the information provided by the full distribution in its high-dimensional parameter space. For example, this distribution contains information about the full covariance of all parameter values with no assumptions about the functional form of the distribution. As an example, Figure 2 shows the one- and two-dimensional marginal distribution of the eight-dimensional ETG model for a Sérsic model. Traditional characterizations of the posterior distribution such as the mean, median, maximum a posteriori probability (MAP) or maximum likelihood (ML) are straightforwardly computed by sorting the converged Markov chain by relative probability value. More general moments requires a density estimate. The BIE provides a high-dimensional kernel density estimator based on a metric tree representation of the Markov chain (e.g. Liu et al. 2006).

Also important and often overlooked are *goodness of fit* diagnostics. A significant goodness of fit error often indicates an inappropriate prior assumption that may include the specified model family itself! The BIE includes a rigorous goodness-of-fit based on Verdinelli & Wasserman (1998). However, this is prohibitively expensive for a large-scale inference campaign on an astronomical image archive. GALPHAT produces difference images for the MAP and ML solutions that provide a quick visual check and a quantitative assessment based on the chi-squared per degree of freedom. Differences between the observed galaxy image and the model image become obvious only when one looks at a relative residual image (see Figure 3). Large residual values and their patterns often suggest the reason for the poor fit. Finally, if we consider several models like Sérsic or Sérsic plus exponential, GALPHAT can evaluate the evidence supporting each given model by calculating the marginal likelihood using the posterior distributions obtained previously.

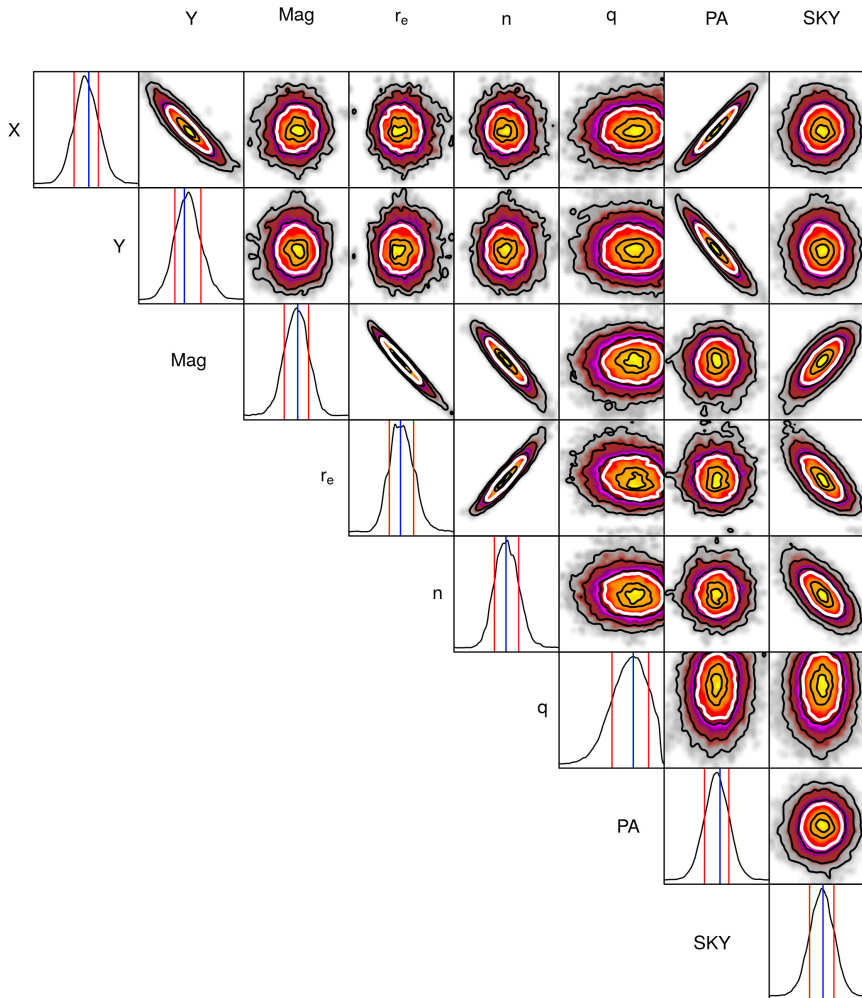


**Figure 2.** One- and two-dimensional marginal distributions of the model parameters for an example Sérsic-model inference. The diagonal contains one-dimensional marginal distributions for each parameter. The blue vertical line shows the position of the MAP value and the red vertical lines show the 1- $\sigma$  range (i.e. the region enclosing 68.3% of the probability). In the off diagonal, the black contours represent the 10, 30, 50, 68.3, 80, 95 and 99% confidence levels and the white solid line is the 68.3% confidence level.

## 2.2. Specification of the prior parameter distribution

Following YWK10, our prior distribution for Sérsic model parameters is based on a combination of linear offsets and multiplicative scalings informed by the quoted catalog parameters and hard limits defined by a detailed visual inspection of fitted galaxy images and previous simulations from (La Barbera et al. 2010). Table 1 shows a typical set of prior distributions used for this work. The *Control* type describes whether the catalog or input value is added to the parameter value (*Additive*), multiplied by the parameter value (*Scaled*), or used directly (*None*). The magnitude is formed from the sum of the supplied catalog magnitude and the parameter value off-

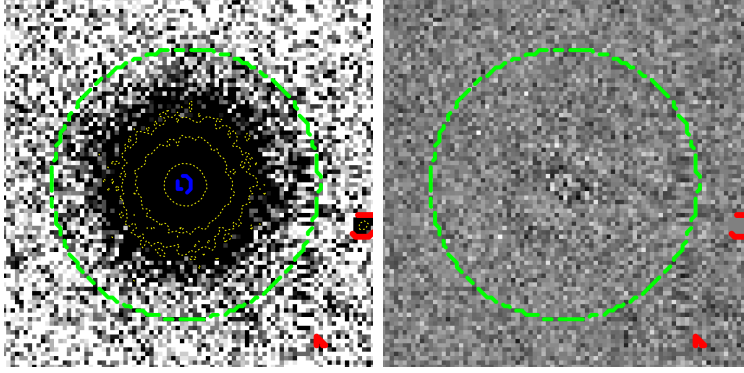


**Figure 3.** SDSS postage stamp of a typical galaxy in r band with  $\text{Mag} = 15.42$ ,  $r_e = 6.97$  arcsec,  $n = 4.53$  (left) and residual images produced by GALPHAT with relative error varying between  $-2.12$  and  $1.85$  % (right).

**Table 1.** Prior specification.

Parameters	Control	Offset	Min	Max	Distribution	Units
X	Additive	$x_c$	-3.0	+3.0	Normal ( $\mu = 0.0, \sigma = 1.5$ )	pixels
Y		$y_c$				
Mag	Additive	PetroMag	-1.0	+1.0	Normal ( $\mu = 0.0, \sigma = 0.2$ )	
$r_e$	Scaled	$r_e$ (deV)	0.33	3.0	Weibull ( $k = 1.21, \lambda = 2.5$ )	pixels
$n$	None	None	0.5	14	Normal ( $\mu = 6.0, \sigma = 6.0$ )	
$q$	None	None	0.09	0.99	Uniform	
PA	Additive	PA (deV)	0.0	0.69	Normal ( $\mu = 0.0, \sigma = 0.69$ )	radians
SKY	Scaled	SKY ( $_{\text{Sex}}$ )	0.97	1.03	Normal ( $k = 1.0, \lambda = 0.01$ )	counts

set by  $-1$ . This offset accommodates skewed prior distributions, such as the Weibull distribution. The offsets for  $x_c$ ,  $y_c$ ,  $r_e$ , PA and Mag are set considering the reference values obtained by SExtractor and the SDSS imaging pipeline (Lupton et al. 2001a).

### 2.3. Computational details

Here, we provide BIE and GALPHAT usage details specific to this project. Additional discussion of the BIE and GALPHAT can be found in Weinberg (2013) and YMK10. In summary, the GALPHAT likelihood function assumes an independent per-pixel Poisson process for all unmasked pixels. Given a model parameter vector, GALPHAT produces a theoretical image with the same geometry as the input *postage-stamp* FITS image and convolved with the provided PSF. As in YMK10, we use the *self-tuning differential evolution* algorithm (Ter Braak 2006) for MCMC posterior sampling and the Gelman-Rubin (Gelman & Rubin 1992) convergence diagnostic. Typical chain swarms have between 16 and 64 members for models with 8 to 12 parameters. In general, fastest throughput is obtained by assigning one chain

to each core. If physical memory is limited, multiple chains may be assigned to each core. We retain at least 100,000 converged chain states for each parameter estimation. Appendix A presents performance statistics.

GALPHAT improves the computational throughput and accuracy by maintaining a nested multi-resolution grid of the two-dimensional flux profiles indexed by model shape parameter(s). YMK10 tested GALPHAT with 3000 synthetic Sérsic galaxy images representative of the 2MASS survey. Their ensemble contains galaxies with shape parameters varying from 0.7 to 7, effective radius ranging from a few arcseconds to 9.37 arcsec ( $8 \times$  the typical FWHM of the PSF) and a sky background of 300 [ADU]. Two multi-resolution levels provide sufficient accuracy. In SDSS, the scatter in the structural parameter distributions are larger, with  $n$  ranging from 2 to 10, and 10% of all galaxies have  $r_e \geq 10$  arcsec (La Barbera et al. 2010) and hence required three multi-resolution levels. The first grid is used to compute the pixel flux for the inner region ( $0.0396 < r_e < 0.396$  arcsec), the second grid for the intermediate region ( $0.396 < r_e < 3.96$  arcsec), and the third is for the outer region ( $3.96 < r_e < 39.6$  arcsec), each one having an image size of  $316.8 \times 316.8$  arcsec,  $594 \times 594$  arcsec, and  $792 \times 792$  arcsec, respectively. The interpolation grids are linearly distributed as a function of  $n$ , ranging from 0.5 to 14.0 with 120, 120, and 240 points for the inner, intermediate, and outer grid respectively. The flux in the central pixels ( $0.0396 \text{ arcsec} < r_e$ ) is computed by adaptive cubature with a strict error tolerance in relative and absolute error of 1 part in  $10^8$ . Although the initial grid computation is time consuming, GALPHAT automatically caches these grids for future use.

Finally, the original GALPHAT algorithm rotated the theoretical image to the desired position angle before convolving with the instrumental PSF. For very high concentration images, however, the three-shear rotation algorithm described in YMK10 can introduce artifacts owing to large relative flux differences between adjacent pixels. To mitigate this problem, the PSF is inversely rotated by the desired position angle and convolved with the non-rotated image. The image rotation is then performed on the smoothed model image.

### 3. ANALYSIS OF SIMULATED IMAGES

#### 3.1. *Motivation and plan*

The Bayesian posterior distributions are not guaranteed to be centered or peaked at the true value for any single parameter or be mutually independent of other parameters. Any preferred one-sidedness for a statistical estimator is referred to as *bias*. This definition is only meaningful for non-Bayesian estimators, because the product of a Bayesian inference is the posterior distribution instead of a single parameter value. Nonetheless, following astronomical tradition, we will want to characterize the inferred parameters by some representative value. This might be the maximum a posterior (MAP), the median, or the mean. We will use the term *bias* here to describe the offset of our chosen characteristic value from the true value for an ensemble of inferences.

The parameters for galaxy surface brightness models are often covariate. For example, consider the task of inferring the parameters for a Sérsic model for a given image. An increase in concentration caused by increasing the Sérsic index  $n$  may be compensated for by increasing the half-light radius to maintain a good fit. Similarly, an increase in half-light radius may be compensated for by a decrease in magnitude. These covariances tend to *stretch* the parameter distributions in various directions. This stretching may be unwittingly interpreted as a true astronomical correlation. Using the full posterior distribution rather than point characterization (such as MAP, ML, mean, etc.) prevents this source of confusion.

Finally, all galaxy image ‘fitting’ packages produce a theoretical image for a particular parameter vector. Computational efficiency demands approximation. Approximation and truncation error in these computed images may result in numerical artifacts that contribute to bias and covariance. Most of the previous studies have used the same model generator routines to create the test images and to estimate the structural parameters. If one uses the same algorithm to produce the test images and compute a comparison image for the objective function, numerical artifacts would tend to match and indicate artificially favorable performance. For example, the numerical algorithms implemented to speed up the inference process like pixel integration, convolution, and rotation become less accurate for very concentrated light distributions, such as those with very high Sérsic indices ( $n \geq 8$ ). When the same procedure is used to generate simulated images for testing, the errors introduced by the numerical methods will be the same and deceptively cancel out.

To characterize the features of our inference, we updated the independent model image generator used in YMK10 to perform the pixel integration using explicit analytic translation and rotation mappings and brute-force two-dimensional quadrature for the point-spread function convolution. This image generator implements a recursive quad-tree cubature scheme with a strict error tolerance to compute the pixel fluxes. This algorithm is too expensive for GALPHAT itself but prevents artificial concordance resulting from using the same algorithm for image generation and image fitting.

YWK10 have shown that GALPHAT recovers the structural parameters with a bias that depends on the image S/N, PSF FWHM, image stamp size and the shape parameter  $n$ . For comparison, we use a simplified definition for signal-to-noise ratio that only includes noise from the astronomical source signal and the sky signal. This could be easily extended to include other instrumental sources including read noise, dark current, etc. We reproduce and extend these results for testing our recent GALPHAT improvements using the PyPiGALPHAT pipeline generator (see Appendix B). For future planning, we use this opportunity to benchmark the GALPHAT performance for a modern survey (see Appendix A). We created various ensemble simulated images, described in Table 2, to extensively test various aspects of GALPHAT under a variety of circumstances: (1) varying  $r_e$  and the shape parameter  $n$  as a function of S/N and PSF FWHM (Ensemble A); (2) varying the position angle (PA) and  $n$  as function of PSF FWHM, and assuming typical values for  $r_e$ ,  $q$  and S/N (Ensemble



B); (3) varying the axis ratio  $q$  as function of PSF FWHM,  $n$  and considering typical values for S/N and  $r_e$  (Ensemble C); (4) varying  $n$  and PSF FWHM, for a comparison between GALPHAT and GALFIT (Ensemble D); (5) galaxies with a real distribution of ETG structural parameters based on the SPIDER project [La Barbera et al. \(2010\)](#) (Ensemble E, see more details in §3.3); and (6) galaxies with central point sources to test the Bayes-factor model classification as a indicator of nuclear activity assuming typical PSF FWHM and S/N (Ensemble F).

**Table 2.** Summary of simulated images ensembles.

Ensemble	Galaxies <sup>a</sup>	$N_{\text{realizations}}$	Parameter	Values
A	1920	2	$r_e$ (")	0.99, 1.98, 2.97, 3.96, 4.95, 7.92, 15.84, 31.68
			PSF FWHM(")	0.75 to 2.14, steps 0.28
			S/N	300, 450, 600, 750
			n	2, 4, 6, 8, 10
			Fixed	q= 0.7, PA = 0 (°)
B	360	2	PA (°)	-60, 0, 30, 60, 90, 120, 150
			PSF FWHM(")	0.75 to 2.14, steps 0.28
			n	2, 4, 6, 8, 10
			Fixed	S/N = 450, $r_e=3.96$ ("), q = 0.7, PA = 0 (°)
			C	600
PSF FWHM(")	0.75 to 2.14, steps 0.28			
S/N	300, 450, 750			
n	2, 4, 6, 8, 10			
$r_e$ (")	0.99, 3.96, 31.68			
Fixed	PA=0 (°)			
D	1200	50 <sup>b</sup>	n	2, 6, 8, 10
			PSF FWHM(")	0.75 to 2.14, steps 0.28
			Fixed	S/N = 450, $r_e=3.96$ ("), q = 0.7, PA = 0 (°)
E	1500	1	n, $r_e$ , q, mag,FWHM	2DPHOT Distribution (see Figure 9)
F <sup>c</sup>	432	1	$\delta\text{Mag}$	3, 5, 7, 8, 9, $\infty^d$
			$r_e$ (")	0.99, 1.98, 2.97, 3.96, 7.92, 15.84
			n	4, 6, 8, 10
			q	0.5, 0.7, 0.9.
			Fixed	PSF FWHM = 1.3 ("), S/N = 450, PA = 0 (°)

<sup>a</sup>The total number of galaxies is  $N_{r_e} \times N_n \times N_{S/N} \times N_q \times N_{PA} \times N_{FWHM} \times N_{\text{realizations}}$ .

<sup>b</sup>50 realizations have been generated for comparison with GALFIT.

<sup>c</sup>An ensemble to test the BF by considering the model Sérsic + Point Source, where

$$\delta\text{Mag} = \text{Mag}_{PS} - \text{Mag}_{\text{Sersic}}.$$

<sup>d</sup>  $\delta\text{Mag} = \infty$  corresponds to a pure Sérsic profile.

### 3.2. Results

Our simulated ensembles of galaxies allow us to measure GALPHAT biases and uncertainties in model parameters, and the dependence of these inferred model parameters on observational conditions such as the point-spread function (PSF) width and the signal to noise. We combine or *pool* our posterior distributions for all galaxy inferences for each range of parameters. Table 3 presents a summary of the differences between GALPHAT’s pooled posterior median ( $1\text{-}\sigma$ ) and the true values as a function of  $n$  and S/N. Let  $R_k$  denote the value of the  $k_{th}$  percentile value for S/N. We divide our SDSS sample into three groups as follows: small ( $R_0 < S/N < R_{10}$ ), medium ( $R_{10} < S/N < R_{90}$ ), and high ( $R_{90} < S/N < R_{100}$ ). The median values for each S/N subgroup in Table 3 were computed for galaxies with effective radii  $2.97 \leq r_e \leq 4.95$  arcsec and PSF sizes between 1.0 arcsec and 1.6 arcsec (subsamples of the ensembles A, B and C). These latter two ranges are typical of the SDSS sample. These are low- to modest-resolution galaxy images. Table 3 shows the offset or *bias* for each parameter of the model. We quote relative values for all quantities except for magnitude (which is already a relative flux value) and position angle (PA). The relative offsets in the position of the galaxy center X, Y, and the SKY background are below  $10^{-3}$ , and the axis ratio bias is below  $10^{-2}$ . For most cases, the Sérsic index, magnitude and effective radii have relative errors smaller than  $10^{-1}$ . Small relative errors indicate that the GALPHAT solution is close to the true value.

Table 3 reveals the expected dependence of the structural parameters on the signal-to-noise value. The relative offset from the true value or *bias* for Mag,  $r_e$  and  $n$  decrease, albeit modestly, as S/N increases. As  $n$  increases from 2 to 10, the bias in  $\Delta n$ ,  $\Delta \text{Mag}$  and  $\Delta r_e/r_{e_{\text{true}}}$  increases weakly; this is also expected because highly concentrated (larger  $n$ ) profiles are more difficult to fit than profiles with lower concentration (smaller  $n$ ). When the measured S/N varies from low (183) to high (432), the bias in  $\Delta \text{Mag}$  decreases by a factor less than 2 for most cases. We can summarize our results as follows: (1) the centroid is determined to order 0.0002 in all cases (e.g. 0.02%); (2) The magnitude is within 0.05 even for low S/N and high Sérsic  $n$ ; (3) the error in half-light radius is within 0.1 pixel in most cases; (4) the relative error in Sérsic  $n$  is less than 0.1 in all cases and often much better; (5) the axis ratio error is within 0.01 in most cases; (6) the position angle (PA) is typically within 0.2 radian except for low S/N and high-concentration (large  $n$ ) cases; (7) the sky value is determined to better than 0.1%.

As discussed in the previous sections, GALFIT is a widely-used galaxy image fitting tool implemented as a  $\chi^2$ -like minimization using the Levenberg-Marquardt algorithm (Peng et al. 2002, 2010). This is a ML estimator. In contrast, the BIE using GALPHAT computes the probability distribution of the parameters in light of the data given the distribution parameters before fitting. The prior distribution includes assumptions based on physical consistency and knowledge of the astronomical problem at hand. Despite the philosophical and algorithmic differences between the frequentist and Bayesian approaches, likelihood functions, and run time performance, we can compare the accuracy of the parameter estimates from each method. To do this,

**Table 3.** Median and  $1\text{-}\sigma$  relative offsets in the bins  $1.0'' < \text{PSF FWHM} < 1.6''$  and considering typical SDSS image sizes ( $2.97 < r_e < 4.95''$ )

S/N	$n$	$\Delta X$ ( $\times 10^{-2}$ )	$\Delta Y$ ( $\times 10^{-2}$ )	$\Delta \text{Mag}$ ( $\times 10^{-2}$ )	$\Delta r_e/r_{\text{true}}$ ( $\times 10^{-2}$ )	$\Delta n/n_{\text{true}}$ ( $\times 10^{-2}$ )	$\Delta q/q_{\text{true}}$ ( $\times 10^{-3}$ )	$\Delta \text{PA}$ ( $\times 10^{-1}$ )	$\Delta \text{SKY}/\text{SKY}_{\text{true}}$ ( $\times 10^{-4}$ )
Low	2	$-0.14 \pm 2.40$	$0.17 \pm 2.30$	$-1.40 \pm 5.0$	$2.6 \pm 9.0$	$3.8 \pm 6.6$	$-3.5 \pm 19.0$	$-3.6 \pm 19.0$	$-1.7 \pm 6.5$
	4	$-1.20 \pm 2.00$	$0.61 \pm 1.80$	$-3.8 \pm 4.9$	$8.2 \pm 8.6$	$7.6 \pm 5.9$	$-11.0 \pm 15.0$	$-11.0 \pm 19.0$	$-4.9 \pm 4.7$
	6	$-0.97 \pm 1.80$	$0.48 \pm 1.70$	$-7.1 \pm 6.0$	$18.0 \pm 14.0$	$12.0 \pm 7.4$	$-13.0 \pm 17.0$	$-13.0 \pm 23.0$	$-6.5 \pm 7.4$
	8	$-0.96 \pm 1.80$	$0.50 \pm 1.80$	$-7.6 \pm 7.7$	$22.0 \pm 22.0$	$13.0 \pm 9.1$	$-14.0 \pm 19.0$	$-19.0 \pm 29.0$	$-7.5 \pm 14.0$
Med	10	$-0.97 \pm 1.80$	$0.49 \pm 1.70$	$-1.7 \pm 9.1$	$7.0 \pm 26.0$	$6.9 \pm 10.0$	$-14.0 \pm 20.0$	$-20.0 \pm 31.0$	$2.4 \pm 22.0$
	2	$-0.08 \pm 1.40$	$0.03 \pm 1.30$	$-1.4 \pm 3.6$	$2.5 \pm 7.8$	$3.7 \pm 5.0$	$-4.0 \pm 12.0$	$-0.34 \pm 9.2$	$-2.2 \pm 7.1$
	4	$-0.66 \pm 1.2$	$0.41 \pm 1.00$	$-1.7 \pm 2.1$	$3.6 \pm 3.7$	$4.3 \pm 2.8$	$-5.2 \pm 9.8$	$-2.0 \pm 8.8$	$-5.2 \pm 4.5$
	6	$-0.58 \pm 1.00$	$0.41 \pm 1.00$	$-3.6 \pm 3.0$	$8.6 \pm 6.7$	$7.1 \pm 3.9$	$-6.8 \pm 11.0$	$-2.5 \pm 9.8$	$-7.8 \pm 6.5$
High	8	$-0.54 \pm 1.00$	$0.35 \pm 0.95$	$-5.7 \pm 4.5$	$15.0 \pm 12.0$	$10.0 \pm 5.5$	$-7.6 \pm 13.0$	$-2.7 \pm 11.0$	$-11.0 \pm 12.0$
	10	$-0.52 \pm 0.96$	$0.34 \pm 0.94$	$-4.7 \pm 5.3$	$14.0 \pm 16.0$	$9.1 \pm 6.4$	$-7.9 \pm 14.0$	$-3.2 \pm 12.0$	$-7.3 \pm 16.0$
	2	$-0.43 \pm 1.20$	$0.24 \pm 0.84$	$-0.15 \pm 0.92$	$0.39 \pm 1.0$	$1.3 \pm 1.4$	$-3.3 \pm 4.6$	$-2.3 \pm 3.6$	$-1.9 \pm 3.4$
	4	$-0.26 \pm 0.78$	$0.11 \pm 0.59$	$-1.9 \pm 1.7$	$3.4 \pm 2.6$	$4.6 \pm 2.4$	$-6.3 \pm 7.1$	$-1.9 \pm 2.5$	$-9.5 \pm 7.3$
	6	$-0.26 \pm 0.72$	$0.09 \pm 0.61$	$-3.1 \pm 2.3$	$6.9 \pm 4.7$	$6.6 \pm 3.3$	$-7.6 \pm 7.8$	$-2.1 \pm 3.0$	$-11 \pm 7.6$
	8	$-0.37 \pm 0.70$	$0.19 \pm 0.63$	$-4.4 \pm 2.6$	$12 \pm 7$	$8.2 \pm 3.7$	$-9.3 \pm 7.4$	$-3.9 \pm 3.8$	$-15.0 \pm 9.9$
	10	$-0.31 \pm 0.71$	$0.22 \pm 0.63$	$-4.2 \pm 2.8$	$13 \pm 8.3$	$8.0 \pm 3.6$	$-9.8 \pm 7.4$	$-3.9 \pm 3.8$	$-10.0 \pm 13.0$

we consider an ensemble of simulated galaxy images that consist of 50 realizations of 24 galaxies with typical values of S/N,  $r_e$ , and  $q$  (ensemble D). We characterize the offset from the true value using the median and quartiles for the pooled posterior distributions for GALPHAT and using the median and quartiles for the ML estimates from GALFIT. This comparison is presented in Figure 4. For low Sérsic index  $n$  (e.g.  $n = 2$ ) the bias in  $n$ ,  $r_e$  and Mag is negligible and both methods work similarly well. For a typical ETG value of  $n = 6$ , we see a tendency of the bias being larger for smaller values of FWHM, but we still see both methods behaving equally well. The most striking difference appears for more extreme values of  $n$ . For  $n = 10$ , GALPHAT biases for  $n$ ,  $r_e$  and mag are  $5.7 \pm 7.9\%$ ,  $7.6 \pm 19\%$ , and  $-0.027 \pm 0.068$  mag, respectively, while GALFIT biases are  $15 \pm 7.4\%$ ,  $22 \pm 19\%$ , and  $-0.088 \pm 0.059$  mag, respectively. These experiments show that GALPHAT’s inference of structural parameters is more accurate than GALFIT’s, especially in the regime of high Sérsic index.

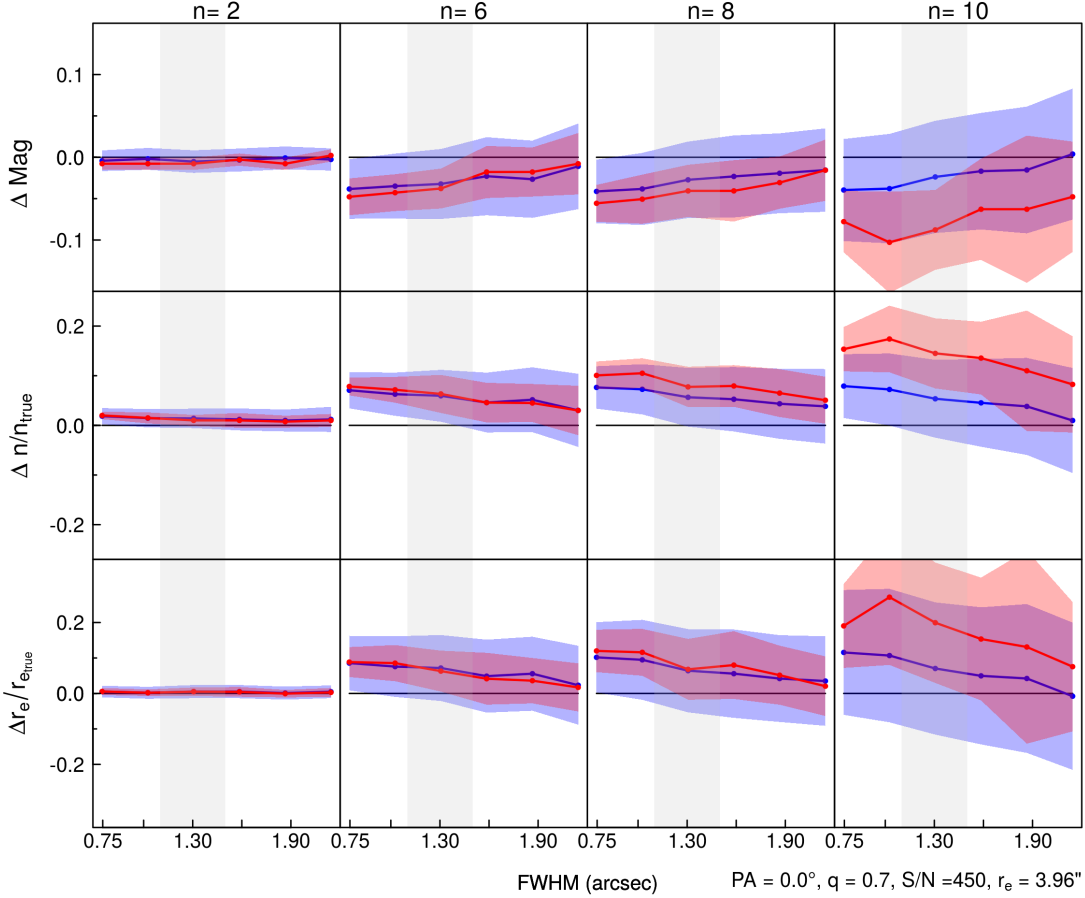


**Figure 4.** A comparison of relative error in GALPHAT and GALFIT for 50 galaxy image realizations. We show the median and the 1- $\sigma$  range (estimated using the interquartile range). Blue lines denote GALPHAT’s pooled posterior medians, and red lines denote GALFIT’s ML medians. The shaded areas indicate expected values for the PSF FWHM in SDSS images based on quartiles.

These results indicate that important scaling relations inferred from structural quantities might be affected by these biases (Bernardi et al. 2003; Shen et al. 2003; Hyde & Bernardi 2009; Bernardi et al. 2017). For instance, we find that the effective radius as estimated by GALFIT can deviate from the true value by as much as 22%. Also, the so called Fundamental Plane (FP) of elliptical galaxies depends critically on an unbiased evaluation of effective radius, luminosity, and velocity dispersion. Deviations of 22% in effective radius can certainly compromise, for example, the study of the origin of the FP as well as its claimed dependence on the environment.

Ideally, one uses the full posterior distribution for prediction and inference. However, this is not feasible for some applications and certainly when comparing to frequentist estimators. We now consider whether the MAP value is sufficient to characterize the error distribution. Ensemble E allows us to compute the the MAP, ML, mean and median error offset. Each of these gives similar results for high values of S/N. As in our previous analysis, we combine or *pool* the GALPHAT posterior distributions for each parameter range of interest to retain the intrinsic covariance. Table 4 illustrates the error offset between the true value and the median MAP and the median of the pooled posterior in bins of S/N. We find that as S/N decreases, the bias increases as expected. We see also that the pooled posterior is slightly less biased than the median MAP value. In short, although we expect the pooled posterior estimates to be provide more information, the median MAP values are adequate.

**Table 4.** Error offsets for 1500 SDSS-like sample

Parameters	Solution	S/N < 183	183 < S/N < 432	S/N > 432
		(Low)	(Intermediate)	(High)
$\Delta\text{Mag}$	Median	$-2.71 \pm 3.44$	$-1.66 \pm 2.16$	$-1.28 \pm 1.09$
	Pooled Posterior	$-2.47 \pm 5.27$	$-1.60 \pm 2.75$	$-1.26 \pm 1.39$
$\Delta r_e / r_{e,\text{true}}$	Median	$4.50 \pm 7.23$	$2.86 \pm 5.18$	$2.64 \pm 2.58$
	Pooled Posterior	$4.44 \pm 11.60$	$2.81 \pm 6.33$	$2.47 \pm 3.28$
$\Delta n$	Median	$3.33 \pm 2.73$	$2.57 \pm 1.95$	$1.74 \pm 1.06$
	Pooled Posterior	$3.31 \pm 4.33$	$2.45 \pm 2.57$	$1.64 \pm 1.21$
$\Delta q / q_{\text{true}}$	Median	$-0.22 \pm 1.55$	$-0.64 \pm 0.95$	$-0.46 \pm 0.66$
	Pooled Posterior	$-0.26 \pm 2.23$	$-0.63 \pm 1.31$	$-0.52 \pm 0.77$

To characterize the quality of GALPHAT’s parameter estimates for a realistic astronomical survey, we generated synthetic images for a sample of 1500 ETGs with parameters randomly extracted from the 40,000 ETGs defined in the SPIDER project (La Barbera et al. 2010). The parameters for each galaxy were derived using 2DPHOT (La Barbera et al. 2008). The resulting sample of 1500 galaxies is Ensemble E in Table 2. Figure 5 illustrates the one- and two-dimensional marginal posterior distributions for the Mag,  $r_e$ , n, q, PA, and the SKY. We divide the ensemble into two subsamples containing 10% of the total sample each: a high signal-to-noise sample with  $S/N > 432.1$  in the lower diagonal and a low signal-to-noise sample with  $S/N < 183.35$  in the upper diagonal. The diagonal contains the one-dimensional



marginals for both subsamples coded by S/N value: black (blue) for low (high) S/N. In all cases, the width of the distribution is smaller for high S/N and peaks close to the true value (shown as a red vertical line). As expected, the half-light radius is covariant with the concentration and magnitude: larger  $r_e$  and/or smaller Sérsic index  $n$  may be compensated for by a smaller MAG. The overall trends are similar with the analysis presented in YMK10 (Figures 5-8).

We now select two subsamples, each containing 10% of the total, as in Figure 5, but selecting on extreme values of Sérsic index; the low-value sample has  $n < 3.35$  (lower diagonal, blue) and high-value sample has  $n > 8.88$  (upper diagonal, black). Figure 6 reveals larger credible intervals for high  $n$  values with similar trends in covariance as described for Figure 5. Figure 7 describes posterior distribution for the lower 10% and upper 10% in half-light radius,  $r_e$ . For small values of  $r_e$ , the wings of the galaxy profile are in the sky and smeared out by the PSF. This decreases the quality of the inferred value of axis ratio  $q$  and Sérsic index  $n$ . These findings are consistent with the previous analysis in YMK10. Figure 8 selects the sample on the lower and upper 10% of the axis ratio distribution. As expected, rounder galaxies, larger  $q$ , have more poorly determined values of position angle PA. The low  $q$  sample is biased toward lower  $q$  values at the 5% level. Conversely, the bias in  $n$  and  $r_e$  is lower for lower axis ratios.

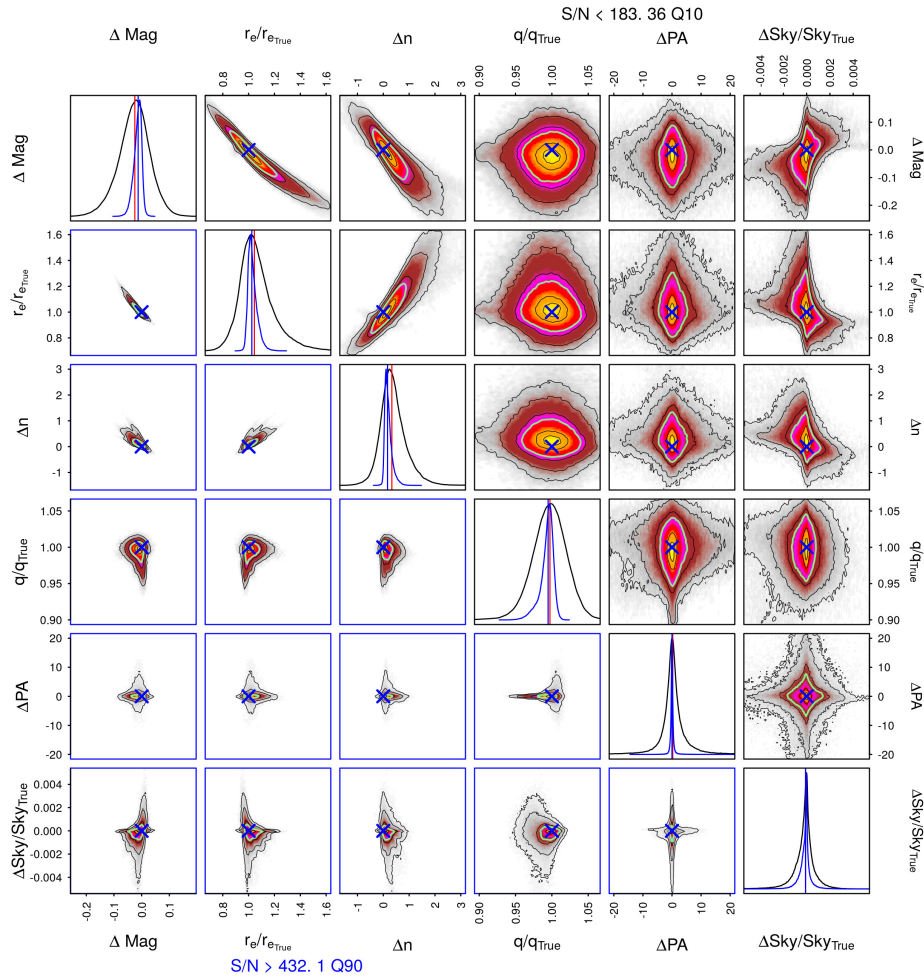


**Figure 5.** The posterior distribution for two subsamples of our simulated ensemble of ETGs for the lower 10% in S/N (upper diagonal) and upper 10% in S/N (lower diagonal). The one-dimensional marginal distributions are shown on the diagonal for low (black) and high (blue) S/N values. The parameters  $r_e$  and  $q$  are scaled by their input values and the other parameters are differences from their true values. The seven contours represent 10, 30, 50, 80, 95, and 99% confidence levels. The light green solid line is the 68.3% confidence level. The locations of the true values are indicated by red vertical lines on the diagonal and cross symbols off the diagonal.

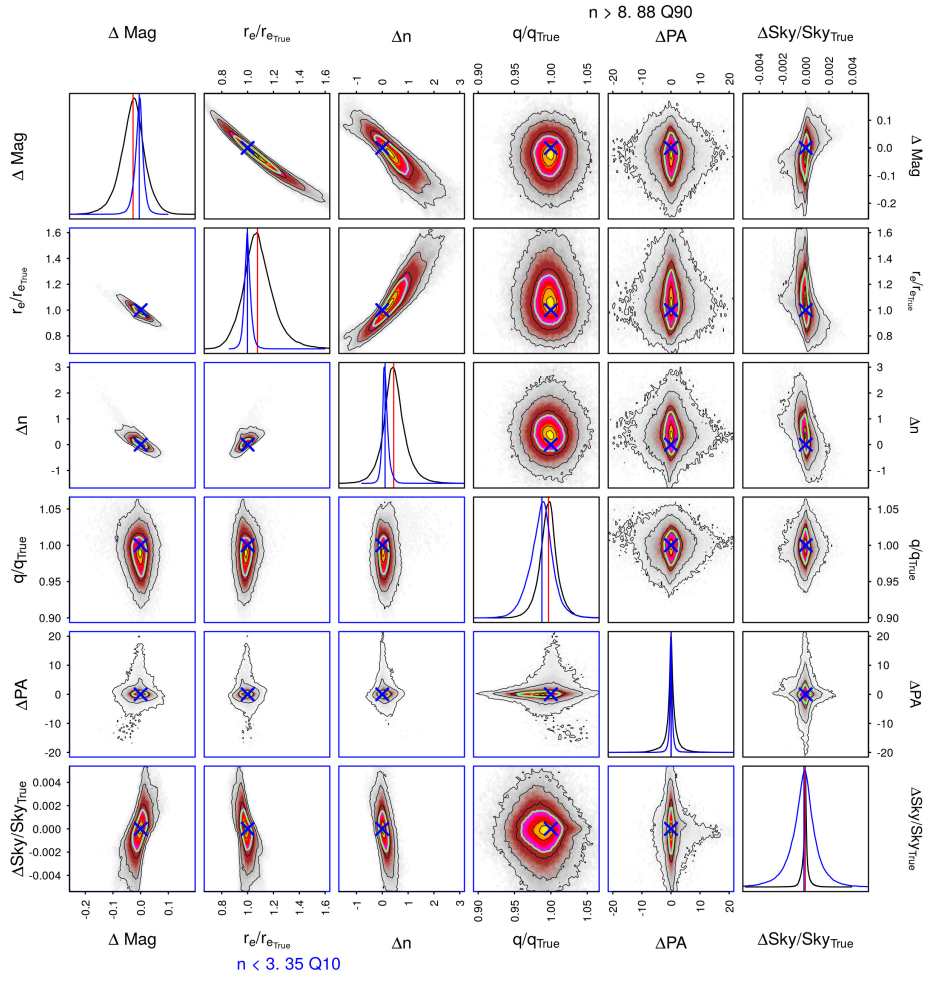


Figure 6. As in Fig. 5 with the lower and upper 10% in Sérsic index  $n$ .

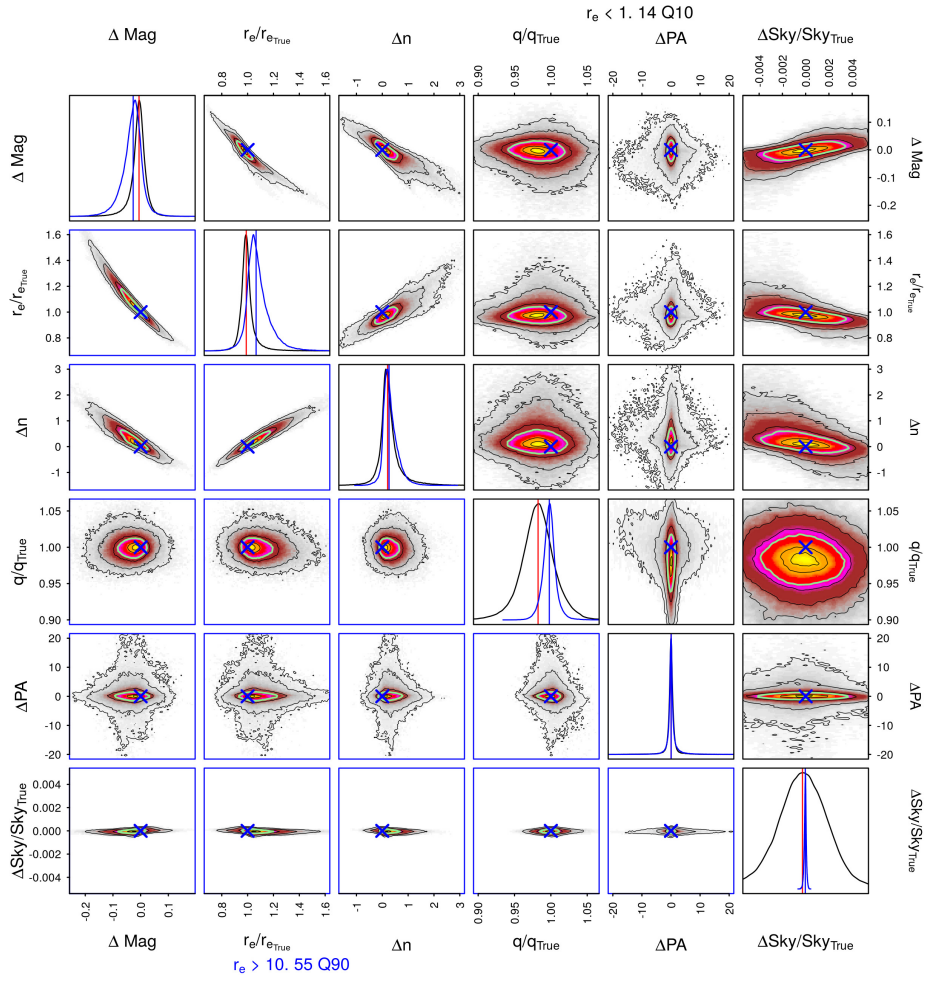


Figure 7. As in Fig. 5 with the lower and upper 10% in half-light radius  $r_e$ .

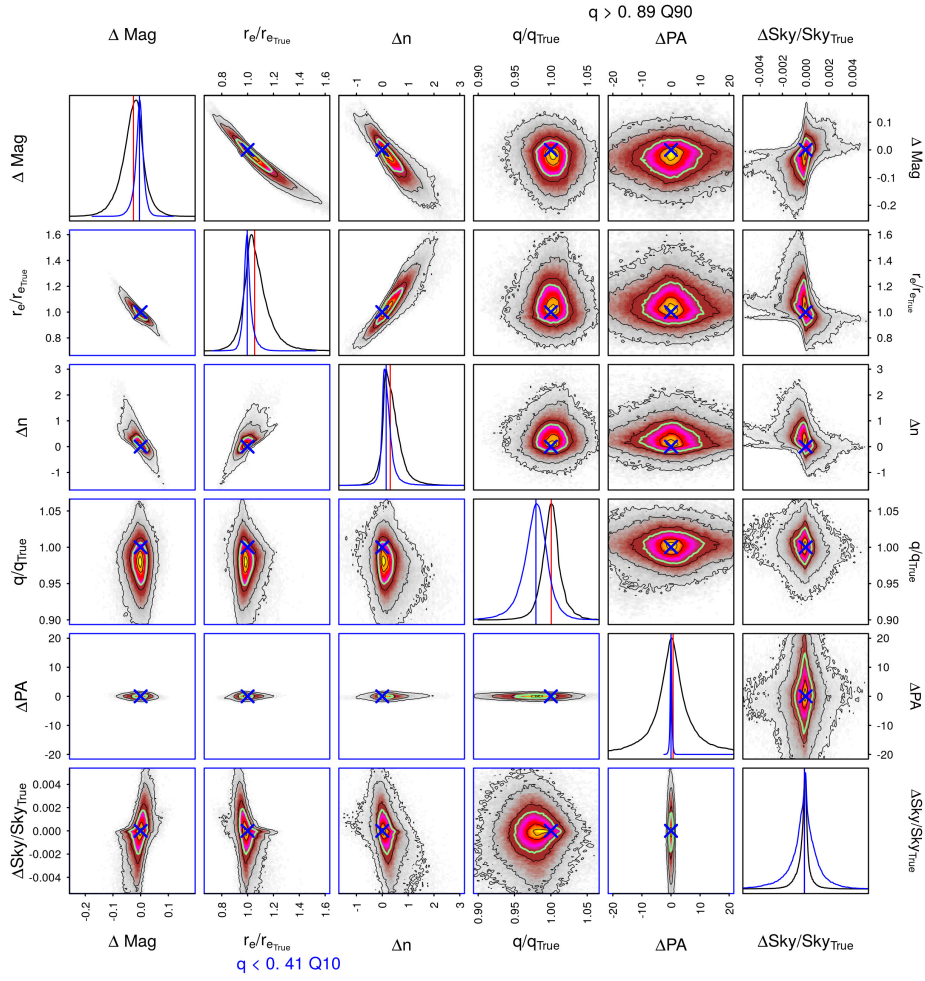
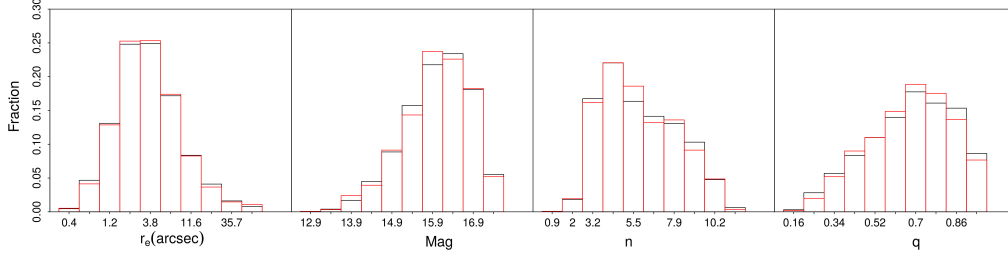


Figure 8. As in Fig. 5 with the lower and upper 10% on axis ratio  $q$ .

### 3.3. Recovery of structural parameters for ETGs

Most astronomical hypotheses are tested using ensemble distributions. Here, we test the recovery of the distribution properties. We simulate this by comparing the marginal distributions of structural parameters (Mag,  $r_e$ , and  $n$ ) inferred by GALPHAT with the original input distribution. Figure 9 illustrates that our subsample of 1500 ETGs have a distribution similar to the SPIDER sample.



**Figure 9.** The distribution of structural parameters found in La Barbera et al. (2010). Black: the distribution of parameters using 2DPHOT (La Barbera et al. 2008) for the 40000 ETGs. Red: the distribution of parameters from GALPHAT for 1500 member random subsample.

For each marginal distribution from the pooled posterior, we compute the Anderson-Darling (AD), and the permutation test p-values. To compare the estimated marginal distributions with the true value distributions, we take 1000 random subsamples from the pooled posterior (1 point from each posterior). Then we apply several statistical tests assuming the null hypothesis that the two samples have identical probability distributions. A permutation test builds a sampling distribution for a statistic (e.g. the mean) by randomly resampling the data and compiling a frequency distribution. If the statistic for the test data set is in the tails of the frequency distribution, we reject the null hypothesis of the same parent distribution. For our experiments, we consider 2000 samples without replacement using the *permTS* package from the R Project (Fay & Shaw 2010).

**Table 5.** Distribution tests p-values for ETG sample

Parameters	Permutation			AD		
	$n_{true}<6$	$n_{true}<8$	$n_{true}<10$	$n_{true}<6$	$n_{true}<8$	$n_{true}<10$
Mag	0.61±0.25	0.60±0.25	0.57 ±0.26	0.75±0.24	0.75±0.24	0.71 ± 0.27
$r_e$	0.61±0.25	0.60±0.26	0.50 ± 0.27	0.69±0.27	0.73±0.25	0.64± 0.28
<b>q</b>	0.24±0.24	0.27±0.26	0.37±0.28	0.36±0.30	0.44±0.29	0.47±0.25
<b>n</b>	0.32±0.26	0.28±0.26	0.07 ± 0.11	0.34±0.27	0.23±0.24	0.07 ± 0.12

Table 5 presents the mean and standard deviation of p-values for the Anderson-Darling (AD) and the permutation tests for all the pooled posterior subsamples for a sequence of cuts in Sérsic  $n$ . Both tests indicate that our pooled posterior subsamples



are similar to the true distributions of  $\text{Mag}$ ,  $r_e$  and  $q$ . The p-values for the Sérsic index distribution, however, are lower, reflecting that only a small number of subsamples (368/355 out of 1000 for the AD/Permutation tests) do not reject the null hypothesis. This is expected because highly concentrated (larger  $n$ ) profiles have significant bias. When we decrease the upper threshold from  $n_{true} < 10$  to  $n_{true} < 8$  the p-value means in the last rows are at least 3 times larger; 774 (863) out of 1000 subsamples now pass the AD (Permutation) test. For  $n_{true} < 6$ , the mean p-values become even larger and more cases pass both tests. Overall, these statistical tests tell us that GALPHAT pooled posterior distributions recover the true value distributions of our synthetic sample.

### 3.4. Inferring the magnitude of central point sources

GALPHAT can be easily extended to model ETGs with a central AGN source as a combination of an extended galaxy light profile and a central point source. The computational challenge is two-fold: (1) a reliable recovery of the point-source magnitude when it exists; and (2) a model comparison test to discriminate galaxies with and without point sources. To test both the reliability of parameter estimation and Bayesian model selection, we generate simulated galaxy images consisting of both a Sérsic profile and a nuclear point source (PS). We assume that this additional component coincides with the galaxy center and is defined by the magnitude of the central point source only,  $\text{Mag}_{PS}$ .

We proceed as in the previous sections: we sample the posterior distribution using BIE and GALPHAT for a model with a point source and a model with no point source. After convergence, the marginal likelihood is computed by the BIE following the algorithm given in Weinberg (2012a) and the extensions discussed in Weinberg et al. (2013). Given a space of models, say  $\{M_1, M_2\}$ , we can use Bayes theorem to compute the relative probability of the model given the data:  $P(M_j|D) = P(M_j)P(D|M_j)/\sum_k P(M_k)P(D|M_k)$ . The relative probability of two models given the same data are then:

$$BF_{12} \equiv \frac{P(M_1|D)}{P(M_2|D)} = \left( \frac{P(M_1)}{P(M_2)} \right) \left( \frac{P(D|M_1)}{P(D|M_2)} \right).$$

The first term is the prior odds ratio, which we typically assume to be unity, and the second term is called the *Bayes factor* (BF). The numerator and denominator in the Bayes factor is exactly the likelihood function marginalized over the prior probability. It is often said that the BF is the relative evidence for two competing models in the data. The evidence in the data favors one hypothesis, relative to another, exactly to the degree that the hypothesis predicts the observed data better than the other. See Kass & Raftery (1995) for more details.

As in the previous section, we will measure the reliability of selecting a Sérsic profile ( $M_1$ ) and a Sérsic profile and a point source ( $M_2$ ) using an ensemble of synthetic images. The PSF FWHM and the pixel scale are fixed by the instrumental and observational conditions of our SDSS sample. Our test ensemble of 432 galaxies covers a wide range of structural parameters designed to assess the limitations of the

BF analysis for identifying a nuclear point source. Of these, 360 of 432 cases have a central point source with varying relative magnitudes,  $\delta\text{Mag}$ , and 72 of 432 cases have a single Sérsic profile. For each combination of effective radius  $r_e$  and Sérsic index  $n$ , we choose discrete values  $\delta\text{Mag}_{\text{true}} = \text{Mag}_{PS_{\text{true}}} - \text{Mag}_{\text{Sersic}_{\text{true}}} = \{3, 5, 7, 8, 9\}$ .

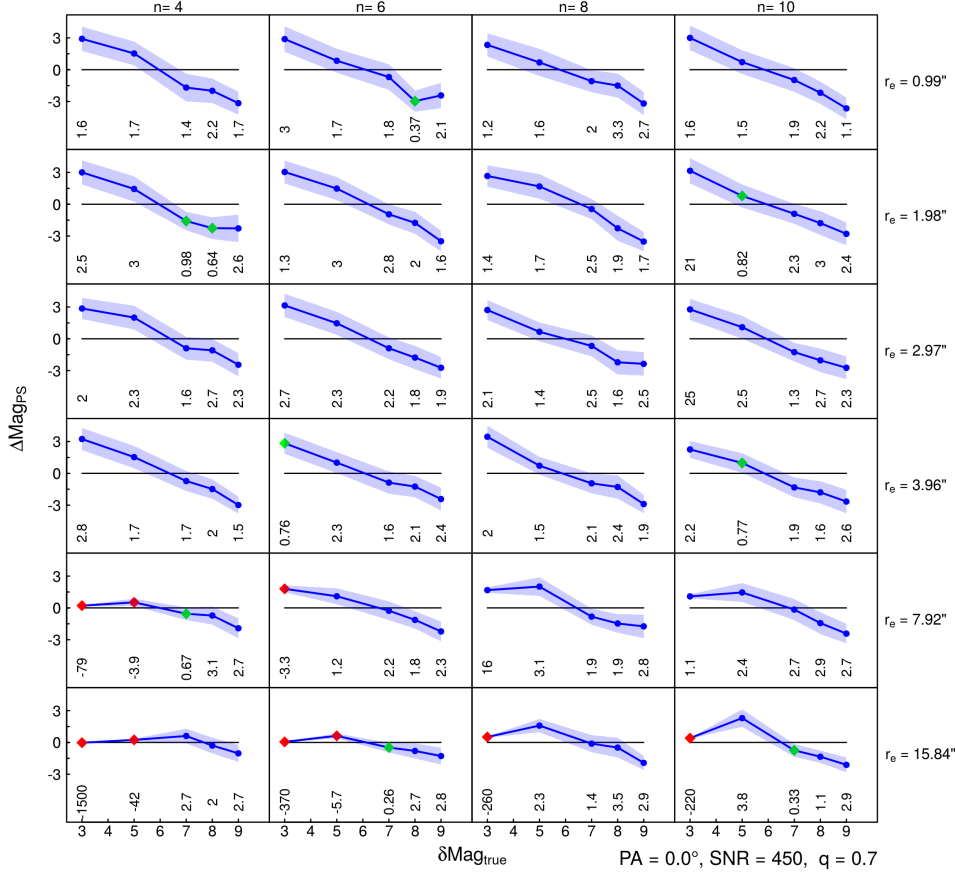


**Figure 10.** Bias in inferred point-source magnitude,  $\Delta\text{Mag}_{\text{PS}}$ , as function of the true magnitude difference,  $\delta\text{Mag}_{\text{true}} = \text{Mag}_{PS_{\text{true}}} - \text{Mag}_{\text{Sersic}_{\text{true}}}$ . Models selected by Bayes factor as containing point sources are indicated in red ( $\ln BF_{12} < -1$ ). Blue points show galaxies where the Bayes factor favors a pure Sérsic model ( $\ln BF_{12} > 1$ ). Green points indicate intermediate cases ( $\ln BF_{12} > -1$  and  $\ln BF_{12} < 1$ ). The solid lines correspond to the posterior median and the shaded area shows the  $1\text{-}\sigma$  quantiles.

For every image, we need to compute separately the posterior distribution under the assumptions of both models,  $M_1$  and  $M_2$ . The value of  $BF_{12}$  required to *believe* either assumption is a matter of cost and risk. Astronomers, because they have a finite amount of expensive data, are willing to take on risk. According to Jeffrey’s interpretation, when  $\ln BF_{12} > 1$  ( $< -1$ ) the evidence is strongly in favor of  $M_1$  ( $M_2$ ). Galaxies in the range  $-1 < \ln BF_{12} < 1$  are considered ambiguous. There are many version of these criteria; see [Kass & Raftery \(1995\)](#) for another commonly used version. When we consider all galaxies without a PS ( $M_1$ ) from the ensemble, the BF correctly prefers model  $M_1$  in 67 of 72 cases; 5 cases were classified as ambiguous and 1 case was incorrectly attributed to model  $M_2$ . Therefore, the reliability obtained is

93.0% and the median and dispersion of  $\ln BF$  for the true  $M_1$  sample are  $2.27 \pm 1.02$ . For galaxies with a nuclear point source, the BF classifies 34 cases of 360 as  $M_2$ . If we define the null hypothesis as *the galaxy does not present a nuclear point source*, false negatives are below 8.3%. Our ability to recover the point-source magnitude in an extended source depends on the  $\delta\text{Mag}_{\text{true}}$ , the ratio  $r_e/\text{FWHM}$  and the Sérsic index  $n$  (see red points in Figure 10). Restricting our sample to images with  $r_e \geq 7.92$  arcsec, for  $n \leq 6$  and  $\delta\text{Mag} \leq 5$  and for  $n > 6$  and  $\delta\text{Mag} \leq 3$ , the false negative rate is  $(2/24) = 8.33\%$  and false positive rate is  $(5/36) = 13.8\%$ . For this experiment, we assume a fixed PSF FWHM of 1.3 arcsec, typical of the SDSS.

Figure 10 illustrates the bias in the inferred  $\delta\text{Mag}$  and the BF as a function of  $\delta\text{Mag}_{\text{true}}$ ,  $n$ , and  $r_e$ . This figure considers typical SDSS values for the S/N = 450 and  $q = 0.7$ . Inspecting the figure rows, one can see that the BF identifies the PS only when  $r_e \geq 7.92$  arcsec, i.e. an effective radius 6 times larger than the FWHM of the PSF. Looking along the columns, as  $n$  becomes larger the BF sensitivity decreases. The PS contribution is negligible when  $\delta\text{Mag} \geq 5$  and GALPHAT returns a finite large value for  $\text{Mag}_{PS}$  even when there is no PS. Therefore, the bias in  $\text{Mag}_{PS}$  decreases as  $\delta\text{Mag}$  increases, i.e. the estimated PS magnitude becomes fainter (cf. the first row in Fig. 10). Finally, the BF can identify the PS only when they are bright enough ( $\delta\text{Mag} < 5$ ), and  $r_e$  is greater than 7.92 arcsec. For  $n = 8$  and  $r_e = 15.84$  arcsec, we can see that the BF detects the PS only for  $\delta\text{Mag} = 3$  or brighter.

**Table 6.** The confusion matrix for point-source selection

	Sérsic	Indeterminate	Sérsic+Point Source	Total
	$\ln BF > 1$	$1 < \ln BF < 1$	$\ln BF < -1$	
Sérsic	21	1	2	24
Sérsic +Point Source	5	0	31	36

To assess the detection and classification errors caused by an offset of the galaxy center from the image center (note that the PS is always at the galaxy center), we created another two samples of synthetic galaxies with point sources. The first sample has the galaxy center at the central pixel of the image, while the second has small shifts from the central pixel. Our experiments have shown that when the galaxy center is slightly shifted (by fraction of a pixel), 43 out of 45 galaxies with  $\ln BF \leq -1$  are still well classified by the BF.

#### 4. APPLICATION TO SDSS ETG IMAGES

We selected early-type galaxies from SDSS DR7 with  $\log M_{\text{stellar}} > 11.50$ , eClass  $< -0.2$  in the redshift range of 0.05 to 0.1 classified as *Elliptical* by the Galaxy Zoo 1 project (Lintott et al. 2011). These are very luminous, high S/N, systems. The threshold in eClass (morphological classification based on the spectrum) usually is set

to zero to discriminate early from late type galaxies, thus setting it to -0.2 minimizes even further any possible contamination from late-type galaxies that may be left from the Galaxy Zoo classification. The minimum redshift reduces aperture effects in the measurements required for the AGN diagnostics (presented in Section 4.1) and the upper limit ensures spectroscopic completeness of the SDSS-DR7. The resulting sample of 200 bright ETGs have all been processed through the SDSS imaging pipeline which fits two models to the two-dimensional image of each object in each band: (i) a pure de Vaucouleurs profile and (ii) a pure exponential profile. Figure 11 shows the effective radius  $r_e$ , the Petrosian magnitudes, and S/N distribution for the sample. We use the catalog values to define the *postage stamp* images and to specify our prior distributions (as described in Sections 2.2 and 2.3 and Table 1). The stamp size was chosen such that the galaxy center is 7.5 de Vaucouleurs effective radii from the stamp edges. We further classify the quality of each image by a quality flag (QF), in Table 7.

GALPHAT produced converged posterior distributions for 166 galaxies out the 200. A detailed inspection of the log files, residuals and posteriors in the 34 unconverged cases indicates that most of them are close to the frame edges (QF=3) and have a secondary object covering the central region (QF=1). All galaxies with QF=0 resulted in converged posterior distributions.

**Table 7.** Postage-stamp quality flags

QF	Description	Count
0	high quality	33
1	close to frame border	31
2	some secondary sources in the outer region	132
3	some secondary sources in the central region	4

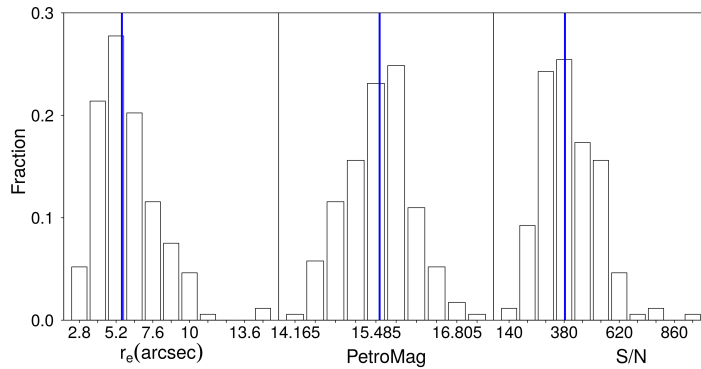


**Figure 11.** Parameter distribution in our SDSS sample: effective radius  $r_e$  (left), Petrosian magnitude (center), and S/N (right). The median values are indicated by the blue vertical lines.

We now select a 102 ETG subsample with  $r_e > 7.92$  arcsec (our *safe* detection limit according to Sec. 3.4) and combine 10000 randomly-selected converged states from the posterior and illustrate the inherent covariance between models (Sérsic and Sérsic plus Point Source) parameters. Using the combined posterior distributions, rather than best-fit ML solutions, we naturally include the intrinsic correlations in the parametric model induced by the data. That is, the posterior distribution will be broadened in the parameter coordinates that suffer intrinsic correlations. Using the posterior sample, rather than a biased single point estimate, allows interesting, subtle details about the entire population to emerge.

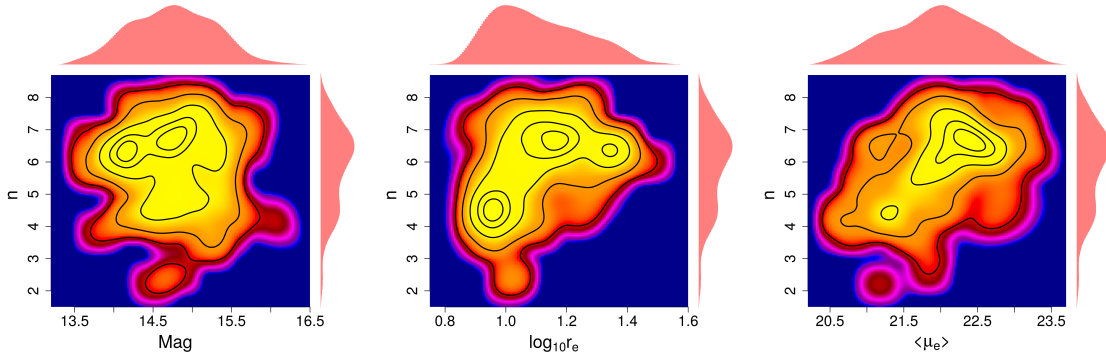


**Figure 12.** Two dimensional distributions of the combined posterior for galaxies with  $r_e > 7.92$  arcsec and  $\ln BF \geq 1$  and  $\ln BF \leq -1$  in our SDSS EGT sample. We combine samples from each posterior weighting by the probability odds.

We combine the information provided by both models (Sérsic and Sérsic plus Point Source), weighting samples from each posterior by the probability odds, e.g.  $w_{i:1,2} = \frac{P(D|M_i)}{P(D|M_1)+P(D|M_2)}$ . Figure 12 shows two-dimensional distributions for various Sérsic-model parameters. The middle panel illustrates the correlation between the Sérsic index and the effective radius and reveals a distinct bimodal distribution. The first mode,  $M_A$ , peaks at  $n \sim 4.5$  and  $\log r_e \sim 0.95$ , and the second,  $M_B$ , peaks at  $n \sim 6.8$  and  $\log r_e \sim 1.15$ . These two peaks seem to also be present in the other two projections, versus magnitude and mean surface brightness. The mean surface brightness at  $M_A$  is significantly higher than at  $M_B$ . This lends further credibility that the bimodal nature of the  $n$  distribution is real.

#### 4.1. AGN classification

We now correlate our 102 ETG subsample with a spectroscopic AGN signature. Our spectroscopic analysis is motivated by the WHAN diagram (Cid Fernandes et al. 2005). This diagnostic diagram uses the  $\log[NII]6584/H\alpha$  ratio and the equivalent width of the  $H\alpha$  line. The main advantage of the WHAN diagram over other diagnostic diagrams (like the Baldwin et al. (1981) diagram) is the ability to separate LINERs from “fake-AGN” – galaxies with low-ionization emission spectra that resemble LINERs but are not caused by nuclear activity. It is, therefore, a useful tool to discriminate between galaxies whose main ionization mechanism owes to main-sequence

high-mass stars (i.e. star-forming galaxies), galaxies where the gas is ionized by active galactic nuclei (Seyfert-like or LINER spectra), LINERs or “retired” galaxies (i.e. galaxies whose emission lines are produced by ionization from hot evolved low-mass stars, HOLMES), and passive galaxies.

Using the CASJOBS interface<sup>2</sup>, we have obtained the equivalent widths and line fluxes of  $H\alpha$  and  $[NII]6584$  from Thomas et al. (2013), derived from the SDSS-III single fiber spectra. These data were available for only 94 ETGs from our  $r_e > 7.92$  arcsec sample. Our *safe* limit assumes a PSF FWHM of 1.3 arcsec.

We find that all galaxies in this subsample have  $\log[NII]6584/H\alpha > -0.4$ . We conclude, therefore, that there are no star-forming galaxies in this sample. This is not surprising given that our sample is composed of massive elliptical galaxies that in general lack active star formation. In the WHAN diagram, the ionization level of non-star forming galaxies is indicated by the equivalent width of the  $H\alpha$  line ( $W_{H\alpha}$ ). An ionization spectrum dominated by active galactic nuclei corresponds to  $\log W_{H\alpha} > 0.48$ , while a passive or *lineless* galaxy is defined by  $\log W_{H\alpha} < -0.52$  and  $W_{[NII]} < -0.52$ ; intermediate values correspond to retired galaxies. Notice that, as shown by Cid Fernandes et al. (2005), there is a considerable scatter around these limiting values.

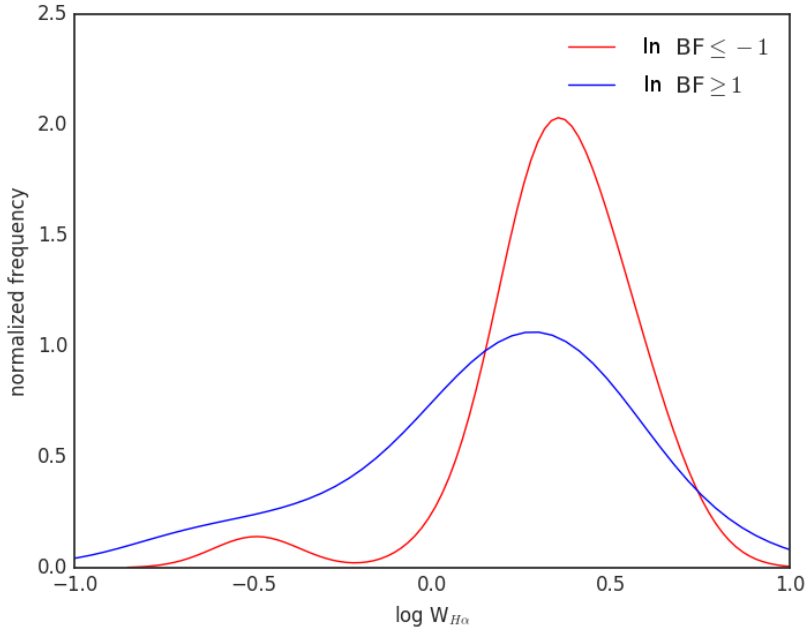


**Figure 13.** Distributions of the  $H\alpha$  equivalent widths (in  $\text{\AA}$ ) for a subsample of ETGs with  $r_e > 7.92$  arcsec. The blue and red lines represent galaxies in the ranges  $\ln BF \geq 1$ , and  $\ln BF \leq -1$  respectively. A Gaussian density kernel has been applied to the discrete data.

<sup>2</sup> <http://skyserver.sdss.org/casjobs/>



Figure 13 presents the distribution of  $W_{H\alpha}$  for our galaxy subsample; a Gaussian density kernel has been applied to the discrete data. We have divided the subsample into three ranges of BF according to the model that best describes the surface brightness distribution: objects for which a Sérsic+PS is favored ( $\ln BF \leq -1$ ), and objects for which a single Sérsic profile is favored ( $\ln BF > 1$ ). Only one galaxy was located in the intermediate region where both models have similar probabilities, and was therefore discarded from further analysis. We can see that the distributions of  $W_{H\alpha}$  are markedly distinct for the two BF ranges. Galaxies with  $\ln BF \leq -1$ , i.e. galaxies for which a Sérsic+PS model is favored, are concentrated around the dividing line between LINERs and retired galaxies, at  $\log W_{H\alpha} \sim 0.35$ . In contrast, galaxies for which GALPHAT does not indicate the presence of a nuclear point source ( $\ln BF \geq 1$ ) are distributed across the full range of the LINER–retired–passive regions. The Anderson-Darling test indicates that the distributions of  $\log W_{H\alpha}$  for galaxies with  $\ln BF \leq -1$  and  $\ln BF \geq 1$  are dissimilar at the 98.6% level.

Low-ionization emission-line regions are present in both AGN, star-forming and non-star-forming galaxies. All of these lead to detectable  $H\alpha$ . The distribution of  $H\alpha$  equivalent width in passive, non-starforming galaxies is broad and extends to low values; the equivalent width in galaxies hosting a modest central emission source is generally larger than approximately  $1 \text{ \AA}$  (e.g. Belfiore et al. 2016). In our sample, there are elliptical galaxies with residual hydrogen being ionized by a number of different sources, be it nuclear or extended in the galaxy. The WHAN diagram suggests that no objects in our sample are star-forming. Therefore, the distribution of  $W_{H\alpha}$  is expected to be broad and extending to low values of  $W_{H\alpha}$  for galaxies identified as single Sérsic profile by GALPHAT. Conversely, even underluminous active nuclei will provide enough ionizing photons to result in a lower floor for WHa. Therefore, the tight distribution for  $\ln BF \leq -1$  and broad distributions for  $\ln BF \geq 1$  are consistent with our photometric identification of central sources.

In summary, Bayes-factor model selection using GALPHAT identifies central point sources when the  $W_{H\alpha}$  is in the vicinity of the LINER/retired dividing line. Conversely, profiles without central point sources (large values of BF) have a broadly extended  $W_{H\alpha}$  distribution, consistent with passive LINERs. Also, GALPHAT does not detect point sources for a significant number of emission-line galaxies where the emission is expected to be extended. This is further evidence that GALPHAT is properly discriminating between galaxies with and without unresolved nuclear emission.

## 5. SUMMARY

We explore the Bayesian inference of the structural parameters for a population of early-type galaxies (ETGs) using the BIE (Weinberg 2013) and GALPHAT. We quantify the accuracy and reliability for extremes in the ETG population and the classification of AGN photometric morphology using Bayes factors. This work introduces a Python-based pipeline, PyPiGALPHAT<sup>3</sup> for automating and documenting

<sup>3</sup> PyPiGALPHAT source code is available on request at [git@bitbucket.org:diegostalder/pygalphat.git](https://git@bitbucket.org:diegostalder/pygalphat.git).

the production posterior distributions on high-performance computing clusters. Our key findings are as follows:

- Using simulated images tuned to SDSS images based on Sérsic profiles, we benchmarked GALPHAT for high,  $4 < n < 10$ , Sérsic index values for the expected ranges of PSF widths and signal-to-noise ratios. The bias in the inference of structural parameters is larger for a concentrated distribution ( $n \geq 8$ ). Our tests extended the parameter space range of the initial benchmarks done by YMK10.
- A comparison between the GALPHAT posterior distribution and GALFIT ML estimates reveals negligible biases for Sérsic  $n \leq 2$  in both methods. The GALFIT bias is significantly larger than GALPHAT bias for higher  $n$  values. For extreme values, e.g.  $n = 10$ , the GALPHAT bias for  $n$  is at least three times lower than the GALFIT bias. The bias for  $n$  is positive, raising the concern that GALFIT can lead to significantly overestimated Sérsic indexes.
- The BIE efficiently estimates the marginal likelihood by resampling (e.g. [Weinberg 2012b](#)), enabling Bayes factor model comparison. We tested the power in Bayes factor selection between pure Sérsic profiles and Sérsic profiles with central point sources. The BF can reliably identify central point sources of galaxies with effective radii larger than 7.92 arcsec PSF FWHM and pixel scales typical of SDSS. For low (high) Sérsic indexes  $n \leq 6$  ( $n > 6$ ), we can identify point sources with magnitudes 5 (3) mag fainter than the extended galaxy. We find that false positive and negative classification errors are below 14%. For a PSF and pixel scale typical of HST, central point sources can be identified in galaxies with a typical effective radii of 3.96 arcsec and  $\delta\text{Mag} \lesssim 5$ .
- The combined posterior density for a well-defined galaxy sample allows us to characterize trends and features that describe that population. For example, we show that our approach automatically reveals a bimodal distribution. The first mode,  $M_A$ , peaks at a Sérsic of index of  $n \approx 4.5$  and the second mode,  $M_B$ , peaks at an index of  $n \approx 6.8$ . In addition, mode  $M_B$  is characterized by a larger effective radius.
- Our Bayes-factor classified point-source detections correlate with AGN spectral signatures. The members of our ETG sample are distributed between the LINER and retired regions of the WHAN diagram. Our pure Sérsic sample has a much broader distribution in  $H\alpha$  equivalent width, going all the way from LINER to retired to passive galaxies. On the other hand, galaxies with point sources are concentrated in the region that separates the LINER and retired regions, as expected for a true central emission source. We show also that the observational condition characterized  $r_e/\text{PSF FWHM}$  can significantly affect the reliability of the analysis.

We have demonstrated that GALPHAT offers several important advantages over other commonly used 2-d galaxy photometry fitting codes. First, GALPHAT pro-

duces the full posterior distribution, not just the maximum likelihood solution, which reduces biases in correlation estimates as demonstrated in [Yoon et al. \(2010\)](#). This allows the trivial computation of credible intervals for any parameter. Secondly, GALPHAT’s rigorous internal error control allows GALPHAT to robustly determine parameter fits without the need to mask out the central regions, as is often required when using GALFIT. The increased accuracy, reduced bias, and our Bayesian approach allows us to simultaneously fit for the background when we fit the galaxy. This facilitates low-bias parameter estimations since the background uncertainty can be strongly covariant with other parameters in many cases ([Häussler et al. 2007](#); [Guo et al. 2009](#); [Robotham et al. 2017](#)). GALPHAT also gives robust and unbiased parameter estimations down to signal to noise ratios of a few, enabling parameter estimation and classification for faint galaxies in surveys like CANDELS ([Grogin et al. 2011](#); [Koekemoer et al. 2011](#)). Finally, by calculating marginal likelihoods and Bayes ratios, GALPHAT naturally presents the odds that one model is favored over another. For example, in both GALPHAT and GALFIT one can fit the galaxy image either using one Sersic component, a Sersic component plus an exponential disk component, or either model with a central point source, but GALPHAT computes the relative probability of the models in light of the data, e.g. using the Bayes ratio.

Our tests have demonstrated that we can achieve a steady-state posterior distribution in a wide range of typical astronomical regimes and that the simulated posterior will include all multiple modes consistent with the prior distribution. Using the posterior distribution, we show that the surface-brightness model will often have correlated parameters and, therefore, any hypothesis testing that uses the ensemble of posterior information will be affected by these correlations. Our results suggest that Bayesian photometric analysis has the ability to discriminate between competing models. In particular, we have demonstrated with low-resolution SDSS data that we can reliably detect AGN photometric signatures as long as the PSF is smaller than to the characteristic scale of the extended light profile. This method will excel at characterizing high-resolution images from upcoming high-resolution ground based and space-based facilities (e.g. TMT, VLT, and JWST).

**Acknowledgments:** DHS acknowledges the financial support from CNPQ scholarship 140913/2013 – 0. The authors acknowledge financial support from FAPESP through a grant 2014/11156 – 4. S. B. R. acknowledges support from FAPERGS. Much of the work presented here was made possible by the free and open R software environment (R Development Core Team 2016). The authors thank to MCTIC/FINEP/CT-INFRA project (grants 0112052700) and the Embrace Program.

## APPENDIX

### A. PERFORMANCE: DATA MANAGEMENT AND RUN TIME

Large input data sets, intermediate data products, configuration files, and posteriors distributions require organization for successful handling. At each step, the pipeline

maintains a list of files that must be saved or deleted. The most important files and their sizes are listed below:

1. Pre-processing: the input FITS image data (the full frame, postage stamps, and masks; 5 MB), configuration files.
2. Processing output: the posterior samples (ascii; 50 MB), MAP and ML image residuals (50 MB), simulation persistence data (1GB), and log files.
  - 2.2 Pre-postprocessing: compressed posterior samples (FITS.gz; 5 MB), image residuals (7 MB), and log files.
3. Postprocessing: the marginal (140 KB) and posterior distribution plots (155 KB), cumulative covariance data (1.4 MB), residual png images (420 KB), and output catalog having the pooled posterior and inferred figures of merit like the MAP, median, and variances etc.

Table 8 shows a summary of disk space that we need for each stage of the pipeline for our SDSS sample of 200 ETGs.

**Table 8.** Data generated on each stage of the pipeline

<i>Step</i>	Disk Space (200 Galaxies)
Data Frames	1 TB
Preprocessing	350 MB
Processing	2.5 TB
Pre-Post-Processing	1.5 GB
Post-Processing	750 MB

Figure 14 describes the total run time of one MCMC simulation and the likelihood marginalization that is used to compute the Bayes factors as function of the  $S/N$  and postage stamp size (in pixels). The total run time was computed using 10 nodes of our CPU cluster. A least square fitted curve is:  $-1.8 \times 10^{-6}x^3 + 2.326 \times 10^{-3}x^2 - 0.1591x + 43.79$

## B. PYPiGALPHAT

The PyPiGALPHAT pipeline is implemented in Python, csh shell, and R. We developed a set of routines and scripts to retrieve the galaxy images from servers, produce the *postage-stamp* images, identify contaminating sources, generate masks, run GALPHAT, and analyze the data products. The pipeline has three modules: (i) pre-processing (ii) processing and (iii) post-processing. Table 9 summarizes the function of each module. The details of the modules will be described in the following sections.

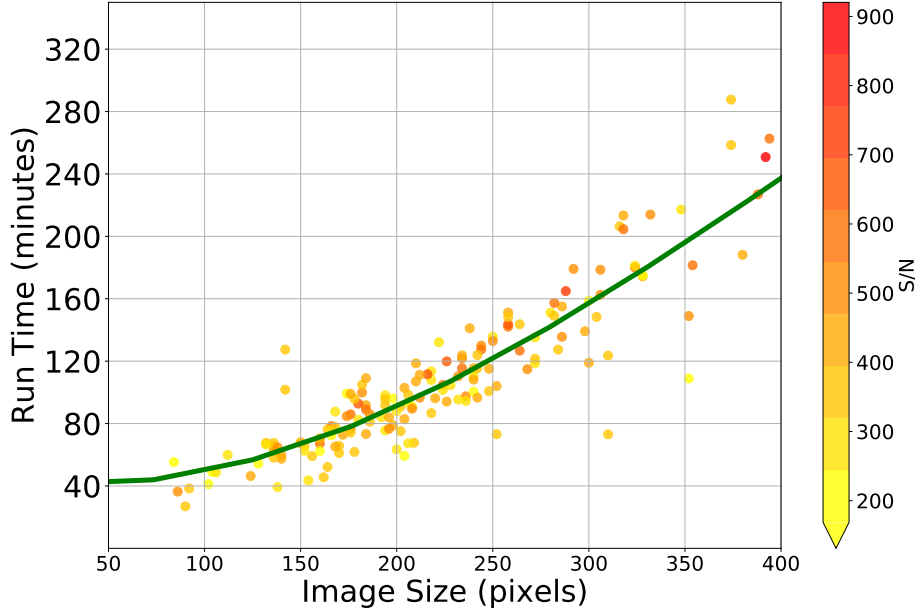


**Figure 14.** Total GALPHAT run time for each galaxy of our SDSS sample. The point colors scale indicate the S/N measured for each galaxy. The green solid lines show a linear least-squares fit.

**Table 9.** PyPiGALPHAT modules

Modules	Stages
Preprocessing	Retrieve data
	Produce image stamps and masks
	Produce GALPHAT input file and script
Processing	Run GALPHAT on HPC hardware
Postprocessing	Quick diagnosis Images
	Generate output catalog

*B.1. Pre-processing: fetching postage-stamp images, producing image masks and generating GALPHAT input files*

The main preparatory steps done by PyPiGALPHAT before estimating the structural parameters using GALPHAT are as follows: (1) build a list with the sky coordinates of the target galaxies; (2) retrieve galaxy metadata from the survey database; (3) download images and PSFs from the survey image server; (4) produce image stamps containing the target galaxies; (5) detect objects in the image stamps and generate preliminary photometric parameters by using SExtractor; (6) generate image masks to exclude non-target features (foreground and background galaxies, diffraction spikes, etc.); (7) produce GALPHAT input files and scripts to obtain structural parameters for a given model (Sérsic, Sérsic plus point source and Sérsic bulge plus exponential

disk); (8) classify the images to produce a quality flag (QF, see Section 4). Many of these details are survey independent and, therefore, minimal changes will be necessary to apply PyPiGALPHAT to another survey. Additionally, PyPiGALPHAT is designed for production with simulated images by simply skipping Steps (2) and (3).

#### B.1.1. Retrieving SDSS Data

We begin by tabulating the exact location of each galaxy, the desired the photometric band (`RA`, `DEC`, `band`). From this list, the pipeline builds SQL queries to retrieve information from the survey data base. Specifically, for the SDSS, we build unique combinations of `ObjIDs`, `run`, `rerun`, `camcol`, `field`. Then, we download the required data files: (i) images having  $2048 \times 1490$  pixels obtained by the photometric data stream from each CCD; (ii) `psFields` which is used to extract the PSF; and (iii) `tsFields` which contains the statistics of the photometric pipeline of SDSS <sup>4</sup>.

The generated SQL query also retrieves a list of photometric parameters (`petroMag`, `petroMagErr`, `rowc`, `colc`, `devRad`, `devVAB`, `devVPhi`) from the SDSS imaging pipeline (Lupton et al. 2001b; Stoughton et al. 2002). This pipeline has been used to analyze the raw telescope images, produce calibrated FITS files, and build catalogs. The main photometric catalog (PHOTO) contains a large number of measured parameters and uncertainties, like the structural parameters assuming a de Vaucouleurs profile.

The PSF spatial variations in SDSS are modeled by the Karhunen-Loève transform (Lupton et al. 2001b). The data file `psFields` has all the information needed to reconstruct the PSF at a desired point in the frame (`rowc`, `colc`). A stand-alone code is available to recover the PSF <sup>5</sup> as an unsigned short FITS file whose background level is set to a standard soft bias of 1000. PyPiGALPHAT removes this soft bias and estimates the PSF FWHM using the function `curve_fit` from `scipy`. Finally, the image stamp and PSF FITS headers are updated with the astrometry and relevant frame keywords.

#### B.1.2. Generating postage-stamp images and masks

The large frames downloaded from the SDSS servers contain multiple objects. During pre-processing, the pipeline script selects a section of the original frame around the target galaxy, producing a *postage stamp*. Each stamp must contain enough pixels to allow for a good estimate of sky background fluctuations beyond the influence of the astronomical source. On the other hand, large stamps increase computational resource requirements. Häussler et al. (2007) have shown that sky estimation is of critical importance to correctly derive the light profiles of galaxies. After several tests and visual inspection of the output images, a linear size of 15 `devRad` per side emerged as a good compromise, where `devRad` is the effective radius produced by the SDSS photometric pipeline assuming a pure de Vaucouleurs law.

The steps required for the image stamp production are as follows: (i) cut out a preliminary stamp with side length of 17 `devRad`; (ii) identify large objects in the

<sup>4</sup> <http://www.astro.princeton.edu/PBOOK/datasys/datasys.htm#astropip>

<sup>5</sup> [http://classic.sdss.org/dr7/products/images/read\\_psf.html](http://classic.sdss.org/dr7/products/images/read_psf.html)

stamp, considering a high detection threshold (more details are given below); (iii) determine the S/N ratio using the isophotal flux (`FLUX_ISO`) and its RMS error (`FLUXERR_ISO`); (iv) estimate the sky background (`SKY`); (v) trim the preliminary image to the final stamp size of `15 devRad`; (vi) identify small objects, considering a lower detection threshold (more details are given below); (vii) extract the information necessary to compute the calibrated flux (`zeropoint`, `airmass`, `extinction coefficient`, `gain`, `readout noise`) from `tsFields` data files<sup>6</sup>; (viii) generate the mask images to avoid non-target objects; (ix) classify the quality of the stamps by generating stamp quality flags (`SQ`) to identify unusual cases.

Each stamp can have photons coming from different objects plus background fluctuations. An accurate estimate of the background level is needed to detect the faintest of these objects. PyPiGALPHAT uses SExtractor (Bertin & Arnouts 1996) to identify these objects in the stamp. The detection threshold is controlled directly by `DETECT_THRESH`, `DETECT_MIN_AREA`, `DETECT_MAXAREA`. For this work, we use the values 1.3, 3.0 and NONE, respectively. Thus, a new source is tagged as independent if it has a flux larger than 1.3 times the standard deviation above the local background and its area is larger than 3.0 pixels. The local background estimate depends on the mesh size (`BACK_SIZE`). PyPiGALPHAT controls this detection threshold indirectly by modifying the mesh size. To detect the larger sources and accurately estimate the background, we set `BACK_SIZE=100`. On the other hand, to identify small sources we consider a finer mesh by setting `BACK_SIZE=10`. PyPiGALPHAT creates mask images from the resulting source list. The masked area is a combination of ellipses centered at the position of each secondary object with centers, axis ratios, and position angles from SExtractor. The axes for each ellipse are scaled by  $3 \times \text{PETRO\_RADIUS} \times \text{A\_IMAGE(B\_IMAGE)}$ . Figure 15 shows a typical stamp and mask produced by the pipeline from an SDSS frame.

<sup>6</sup> <http://classic.sdss.org/dr7/algorithms/fluxcal.html>



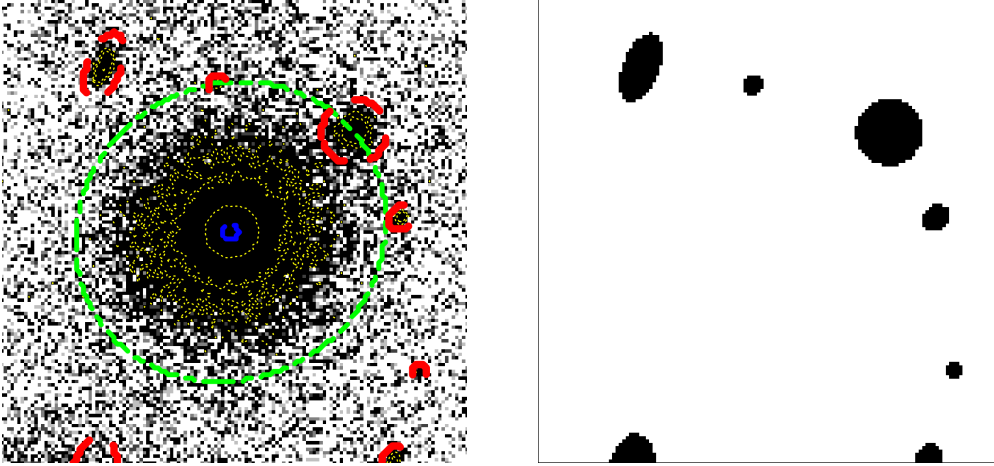


**Figure 15.** Left (Right) panel shows a typical SDSS diagnostic Stamp (mask) obtained by the PyPiGALPHAT preprocessing step. Dotted light green contours indicate the target source. Dotted red lines show mask objects.

Finally, the SQ flag is assigned based on the position of the secondary objects relative to the target galaxy. Let  $R_i$  be the distance from the secondary object to the target. We assign  $SQ = 3$  if a secondary object overlaps the central region, i.e.  $R_i < FWHM$ . We assign  $SQ = 2$  if a secondary object is in the unmasked region with  $R_i > FWHM$  and  $R_i < \text{target major axis}$ . We assign  $SQ = 1$  if we can not create a square image stamp with  $15 \times \text{deVrad}$  on a side (see some examples in Figure 16) without intersecting the frame border. The SQ values are summarized in Table 10.

**Table 10.** Stamp quality flag (SQ)

CRITERIA	NAME	Flag
Clean stamp	OK	0
Galaxy objective close to the FRAME edges	BORDER	1
Secondary objects over the source	OVERLAP_SOURCE	2
Secondary objects over the central region	OVERLAP_CENTRAL	3

### B.2. Running GALPHAT on a HPC cluster

PyPiGALPHAT reads the input galaxy catalog and submits the jobs to the HPC cluster. Each job is responsible for the processing of one galaxy. By default, PyPiGALPHAT will process all galaxies in the input file, but the user can optionally choose a single galaxy from the list, e.g. using the SDSS `objid`. There are three running modes: (1) perform a new inference; (2) resume a pre-stored inference; and (3) run the pre-postprocessing steps to verify successful completion. This last mode identifies the stages of the pipeline that have failed and reruns the inference if necessary.

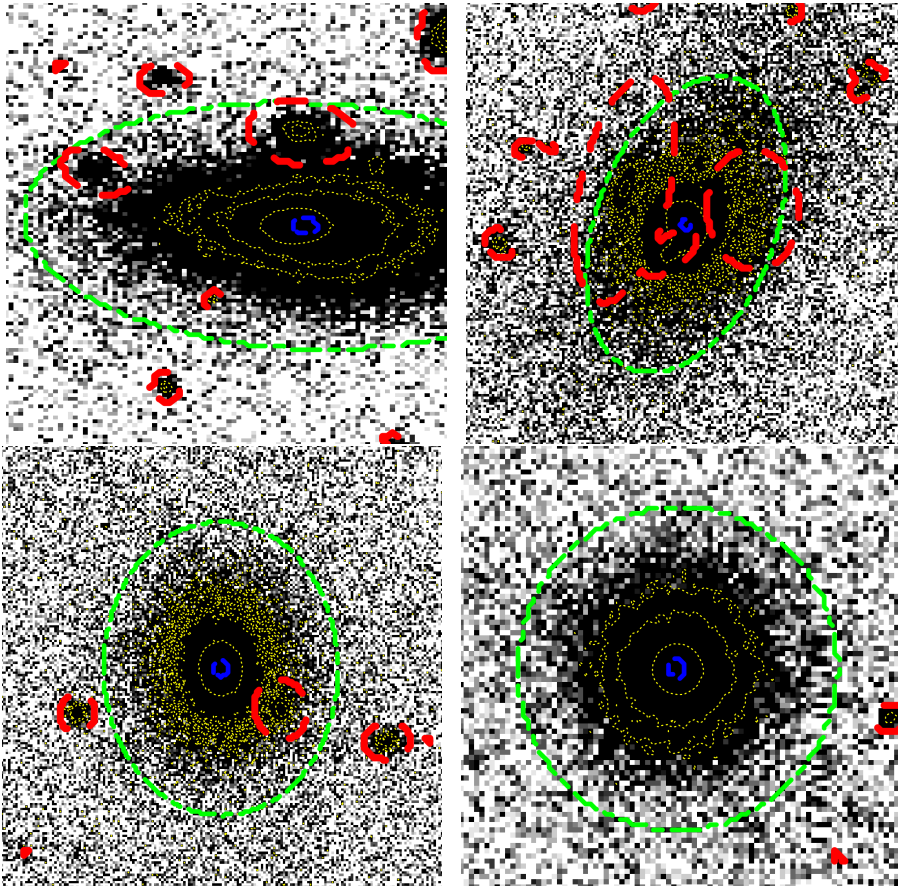


**Figure 16.** From left to right, this figure shows examples for each SQ. The first image corresponds to a galaxy that is close to the frame border (SQ = BORDER); the second one to a galaxy contaminated by secondary sources extending to the central region (SQ = OVERLAP\_CENTER); the third one to a galaxy where a secondary object is inside the green ellipse but does not overlap with the central region (SQ = OVERLAP\_SOURCE). Finally, the last figure shows a clean image (SQ = OK). Dotted red lines indicate the secondary source masked area. Dotted green lines indicate the objective galaxy.

The posterior sample of approximately 100,000 states generated by the MCMC inference needs to be managed efficiently. The ASCII state files are converted to Flexible Image Transport System (FITS) in binary table format. The pre-postprocessing step removes unnecessary log files for successful inferences. When using the multiple-chain differential evolution algorithm, some chains become stuck in regions of anomalously low posterior probability. These chains may be identified and trimmed from the posterior sample using an outlier detection scheme provided by the BIE. PyPiGALPHAT has the option to perform parameter estimation with GALFIT for comparison. The PyPiGALPHAT produces the setup, processes, and validates the results obtained by GALFIT.

### B.3. Output catalogs and diagnostic plots

PyPiGALPHAT provides preliminary analysis of each posterior distribution. Each job is responsible for the postprocessing of one galaxy. Each job calls a `R script`<sup>7</sup>, which has been developed to obtain the diagnostic figures and catalogs with inferred values (e.g. MAP, ML, Median, Mean), pooled posteriors, and covariances.

Galaxies with a low quality flag (QF=1 or QF=3; see Table 1) can converge to incorrect stationary solutions. To detect this and other anomalous conditions, each parameter in the posterior sample is offset and rescaled according to the prior specification defined in Table 1. The one-dimensional marginal distribution and the quantiles 25% and 75% ( $Q_{25}$  and  $Q_{75}$ , respectively) are computed for all model parameters, as well as the MAP and ML solutions. These inferred values can be used to estimate the variance from the interquartile range ( $\sigma = 0.74(Q_{75} - Q_{25})$ ).

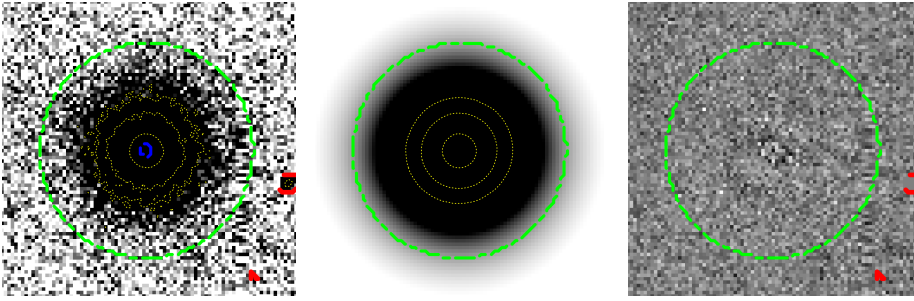


**Figure 17.** Left: an observed Stamp of a given galaxy. Green (red) dotted lines indicate the Petrosian region and the nearby secondary objects. Middle: a model image corresponding to the MAP solution. Right: the MAP residual that corresponds to the difference between the observed and model images, normalized by observed stamps.

Figure 17 shows the postage stamp, the model image, and the residual image of a galaxy considering MAP solutions. These images can help to rapidly identify problematic situations, e.g. incorrect centering or orientation (position angle), mask files missing a secondary source, etc. For each residual image we compute their extreme values, mean and RMS values, which are then saved in the output catalog. All inferred quantities like quantiles, MAP and ML solutions, covariances, likelihood marginalization, and residual extreme values are saved in a final catalog.

## REFERENCES

- Baldwin, J. A., Phillips, M. M., & Terlevich, R. 1981, *PASP*, 93, 5
- Barden, M., Häußler, B., Peng, C. Y., McIntosh, D. H., & Guo, Y. 2012, *MNRAS*, 422, 449
- Belfiore, F., Maiolino, R., Maraston, C., et al. 2016, *MNRAS*, 461, 3111
- Bernardi, M., Fischer, J.-L., Sheth, R. K., et al. 2017, *ArXiv e-prints*, arXiv:1702.08527
- Bernardi, M., Sheth, R. K., Annis, J., et al. 2003, *AJ*, 125, 1866
- Bertin, E., & Arnouts, S. 1996, *A&AS*, 117, 393

<sup>7</sup> <https://www.r-project.org/>

- Bouché, N., Carfantan, H., Schroetter, I., Michel-Dansac, L., & Contini, T. 2015, *AJ*, 150, 92
- Bruce, V. A., Dunlop, J. S., Mortlock, A., et al. 2016, *MNRAS*, 458, 2391
- Capetti, A., & Balmaverde, B. 2007, *AA*, 469, 75
- Cid Fernandes, R., Mateus, A., Sodré, L., Stasińska, G., & Gomes, J. M. 2005, *MNRAS*, 358, 363
- de Vaucouleurs, G. 1948, *Annales d'Astrophysique*, 11, 247
- Erwin, P. 2015, *ApJ*, 799, 226
- Faber, S. M., Tremaine, S., Ajhar, E. A., et al. 1997, *AJ*, 114, 1771
- Fay, M. P., & Shaw, P. A. 2010, *Journal of statistical software*, 36, i02
- Gelman, A., & Rubin, D. B. 1992, *Statistical Science*, 7, 457
- Grogin, N. A., Kocevski, D. D., Faber, S. M., et al. 2011, *ApJS*, 197, 35
- Guo, Y., McIntosh, D. H., Mo, H. J., et al. 2009, *MNRAS*, 398, 1129
- Häussler, B., McIntosh, D. H., Barden, M., et al. 2007, *ApJS*, 172, 615
- Ho, L. C., Filippenko, A. V., & Sargent, W. L. W. 2003, *ApJ*, 583, 159
- Ho, L. C., & Peng, C. Y. 2001, *ApJ*, 555, 650
- Hong, J., Im, M., Kim, M., & Ho, L. C. 2015, *ApJ*, 804, 34
- Hyde, J. B., & Bernardi, M. 2009, *MNRAS*, 394, 1978
- Jeffreys, H. 1961, *Theory of Probability*, 3rd edn. (Oxford University Press USA)
- Kass, R. E., & Raftery, A. E. 1995, *Journal of the American Statistical Association*, 90, 773
- Koekemoer, A. M., Faber, S. M., Ferguson, H. C., et al. 2011, *ApJS*, 197, 36
- La Barbera, F., de Carvalho, R. R., de la Rosa, I. G., & Lopes, P. A. A. 2010, *MNRAS*, 408, 1335
- La Barbera, F., de Carvalho, R. R., de La Rosa, I. G., et al. 2010, *MNRAS*, 408, 1313
- La Barbera, F., de Carvalho, R. R., Kohl-Moreira, J. L., et al. 2008, *PASP*, 120, 681
- Lintott, C., Schawinski, K., Bamford, S., et al. 2011, *MNRAS*, 410, 166
- Liu, T., Moore, A. W., & Gray, A. 2006, *Journal of Machine Learning Research*, 7, 1135
- Lupton, R., Gunn, J. E., Ivezić, Z., Knapp, G. R., & Kent, S. 2001a, in *Astronomical Society of the Pacific Conference Series*, Vol. 238, *AstronomicalData Analysis Software and Systems X*, ed. F. R. Harnden, Jr., F. A. Primini, & H. E. Payne, 269
- Lupton, R., Gunn, J. E., Ivezić, Z., Knapp, G. R., & Kent, S. 2001b, in *Astronomical Society of the Pacific Conference Series*, Vol. 238, *AstronomicalData Analysis Software and Systems X*, ed. F. R. Harnden, Jr., F. A. Primini, & H. E. Payne, 269
- Mancone, C. L., Gonzalez, A. H., Moustakas, L. A., & Price, A. 2013, *PASP*, 125, 1514
- Mendel, J. T., Simard, L., Palmer, M., Ellison, S. L., & Patton, D. R. 2014, *ApJS*, 210, 3
- Peng, C. Y., Ho, L. C., Impey, C. D., & Rix, H.-W. 2002, *ApJ*, 124, 266
- . 2010, *ApJ*, 139, 2097
- Ravindranath, S., Ho, L. C., & Filippenko, A. V. 2002, *ApJ*, 566, 801
- Robotham, A. S. G., Taranu, D. S., Tobar, R., Moffett, A., & Driver, S. P. 2017, *MNRAS*, 466, 1513
- Sérsic, J. L. 1963, *Boletín de la Asociación Argentina de Astronomía La Plata Argentina*, 6, 41
- Shen, S., Mo, H. J., White, S. D. M., et al. 2003, *MNRAS*, 343, 978
- Simard, L. 1998, in *Astronomical Society of the Pacific Conference Series*, Vol. 145, *Astronomical Data Analysis Software and Systems VII*, ed. R. Albrecht, R. N. Hook, & H. A. Bushouse, 108
- Simard, L., Mendel, J. T., Patton, D. R., Ellison, S. L., & McConnachie, A. W. 2011, *ApJS*, 196, 11
- Stoughton, C., Lupton, R. H., Bernardi, M., et al. 2002, *AJ*, 123, 485

- Ter Braak, C. J. F. 2006, *Stat. Comput.*, 16, 239
- Thomas, D., Steele, O., Maraston, C., et al. 2013, *MNRAS*, 431, 1383
- Verdinelli, I., & Wasserman, L. 1998, *Annals of Statistics*, 26, 1215
- Vikram, V., Wadadekar, Y., Kembhavi, A. K., & Vijayagovindan, G. V. 2010, *MNRAS*, 409, 1379
- Wakefield, J. 2013, *Bayesian and Frequentist Regression Methods*, Springer Series in Statistics (Springer New York)
- Weinberg, M. D. 2012a, *Bayesian Analysis*, 7, 737
- . 2012b, *Bayesian Anal.*, 7, 737
- . 2013, *MNRAS*, 1, 1471
- Weinberg, M. D., Yoon, I., & Katz, N. 2013, *ArXiv e-prints*, arXiv:1301.3156
- Yoon, I., Weinberg, M. D., & Katz, N. 2010, *MNRAS*, 414, 1625